Leo van Wüllen*, Jan Gerrit Schiffmann, Jakob Kopp, Zhongqing Liu, Holger Kirchhain, Andre Düvel and Paul Heitjans*

Development and application of novel NMR methodologies for the in situ characterization of crystallization processes of metastable crystalline materials

DOI 10.1515/zkri-2016-1975
Received June 10, 2016; accepted September 6, 2016; published online November 8, 2016

Abstract: In this contribution we report on the development and application of modern NMR approaches for the in situ characterization of the crystallization of metastable materials. The work was performed within the framework of the DFG priority programme SPP 1415 "Crystalline Non-Equilibrium Phases". As one of the goals of this project, the development of a NMR methodology which enables an analysis of local structural motifs on short (1–2 Å) and extended (2–6 Å) length scales without the need for fast magic angle spinning (MAS) has been defined, since the enormous centripetal forces which occur during fast sample rotation (up to 10^7 g) may intervene with the chemical or physical process which is being monitored. To achieve this goal, we developed a magic angle turning probe and pulse sequences allowing to trace the isotropic chemical shifts and heteronuclear dipolar couplings and hence the determination of structural motifs on short and intermediate length scales. With the implementation of novel inductive heating approaches the range of accessible rotation frequencies for in situ high temperature NMR measurements has been enlarged, now covering the ν_{MAS} range of 0–10 kHz with an accessible temperature of up to 700 °C. Application of NMR methodologies for the characterization of crystallization processes and the structure and dynamics of novel phases, partially in joint collaborations within the priority program, are also reported.

Keywords: crystallization processes; ionic conductors; solid state NMR.

***Corresponding authors: Leo van Wüllen,** Institut für Physik, Universität Augsburg, Universitätsstr. 1, 86159 Augsburg, Germany, E-mail: leo.van.wuellen@physik.uni-augsburg.de; and
Paul Heitjans, Institut für Physikalische Chemie und Elektrochemie, Leibniz Universität Hannover, Callinstr. 3 – 3a, 30167 Hannover, Germany, E-mail: heitjans@pci.uni-hannover.de
Jan Gerrit Schiffmann, Zhongqing Liu and Holger Kirchhain: Institut für Physik, Universität Augsburg, Universitätsstr. 1, 86159 Augsburg, Germany
Jakob Kopp: Institut für Physikalische Chemie, Universität Münster, Corrensstr. 28 -30, 48149 Münster, Germany
Andre Düvel: Institut für Physikalische Chemie und Elektrochemie, Leibniz Universität Hannover, Callinstr. 3 – 3a, 30167 Hannover, Germany

Introduction

Solid state nuclear magnetic resonance spectroscopy has developed into one of the most powerful methods for the structural characterization of local structural motifs on short (1–2 Å) and intermediate (2–6 Å) length scales during the last two decades. Especially in systems which are lacking translational periodicity or exhibit a high degree of disorder, solid state NMR spectroscopy can contribute significantly to the identification of local structural motifs, such as coordination polyhedra, connectivity patterns, etc. Especially the introduction of magic angle spinning (MAS) [1, 2] enabled the identification of the immediate bonding environment of the investigated nuclear species, allowing e.g. to quantitatively identify borate, phosphate or silicate polyhedra with different coordination numbers. Novel methods such as multiple quantum MAS (MQMAS) [3–7] or related methods such as satellite transition MAS (STMAS) [8–10] or satellite transitions acquired in real time MAS (STARTMAS) [11] proved to be helpful in the case of nuclei exhibiting a strong second order quadrupolar interaction.

These and related methods have found countless applications in the study of ceramics, glasses and framework structures such as aluminophosphates or zeolites and contributed enormously to the study of the local structural motifs in these materials [12–31].

Structural motifs on a length scale of 2–6 Å may be analyzed via an exploration of the homo- or heteronuclear dipole coupling interactions between pairs of nuclei – these scale with the inverse cube of the internuclear

distance – under the high resolution conditions of fast MAS. A large variety of advanced methods to quantitatively determine the homo- and heteronuclear dipolar couplings and to analyze these with respect to distance sums and geometries have been introduced over the last two decades. These studies provide detailed information about the connectivity motifs in solid materials and about the spatial distribution of chemical species. Methods for the analysis of the homonuclear dipole couplings such as 2D exchange [32, 33], 2D radio frequency driven recoupling (2D-RFDR) [34, 35] or 2D-double quantum NMR experiments [36–38] as well as rotational echo double resonance (REDOR) [39–41] and related methods [42–44] for the analysis of the heteronuclear dipolar couplings contributed enormously to the identification of connectivity motifs in solids [45–49] and found their way into the standard inventory of solid state NMR spectroscopy. Alternative approaches tracing the homo- and heteronuclear scalar J-couplings and thus directly proving the existence of chemical bonds between the involved nuclei have been developed more recently. Approaches which are well established in liquid state NMR such as INEPT, INADEQUATE, HMQC or COSY could be successfully adapted to solid state NMR by Fyfe, Emsley, Massiot and others [50–57].

All these methods, however, rely on the averaging due to MAS, resulting in well-resolved lines which allow for the separation and identification of the various species present in the sample under investigation. In cases in which the MAS process is incompatible with the problem to be studied (e.g. in the case of the study of real catalytic processes or if the fast MAS process may intervene with the physical or chemical process under study) the results obtained from such an MAS experiment may not be representative for the studied process itself. When studying the crystallization of a boron-containing zeolite Freude and coworkers [58] observed that the crystallization rate slows down by an order of magnitude when observing the crystallization under MAS, compared to the crystallization of a non-spinning, but otherwise identical sample. One has then to resort to static, non-spinning conditions resulting in broad lines which usually renders a straightforward and unequivocal assignment impossible, thus severely aggravating the analysis. A NMR methodology which would allow to characterize not only the structural motifs on a length scale of 1–2 Å via an evaluation of the isotropic chemical shift information but in addition provide information about extended structural motifs (2–6 Å), albeit without the need of fast sample spinning therefore would significantly widen the inventory of solid state NMR spectroscopy. The development of such an approach marks one of the goals of this project within the priority program [59].

Another point in which the available approaches are rather limited pertains to MAS experiments at high temperatures and high spinning speeds. Indeed, methods are available allowing MAS experiments at temperatures of up to 800 °C, however, the MAS frequency is limited to ca. 4–5 kHz. This, especially in the case of disordered or amorphous samples which exhibit quite a distribution of isotropic chemical shift values, renders a considerable overlap of center- and spinning sidebands. This severely complicates a straightforward analysis of, e.g. crystallization processes of phosphate phases from an amorphous matrix (vide infra) or the evaluation of chemical exchange processes via an analysis of the temperature dependent evolution of the MAS NMR line shape.

In further activities within the priority program modern NMR methodologies were applied to aid in the characterization of the first steps of the crystallization of novel metastable phases and for the characterization of the structure and dynamics of these novel phases [60–63]. Among the various materials studied, two systems representing ion conductors were studied in detail. The crystallization of lithium aluminogermano phosphate (LAGP) from an amorphous matrix, either prepared via melt-quench or sol-gel processing – results in a material exhibiting extremely promising properties in terms of mechanical stability, electrochemical performance and ionic conductivity. Starting formally from the Al free parent compound, lithium germanophosphate (LGP) the replacement of Ge with Al/Li introduces excess Li which then exhibits extreme Li mobility. However, the details of the crystallization of these phases from the amorphous phase and the details of structure and Li transport in these materials are only partially understood and have been investigated in detail within this project. Specifically, we will report a detailed study of the structural evolution in these materials upon annealing from dipolar MAS NMR experiments such as ^{27}Al{^{31}P}-REDOR, ^{31}P{^{27}Al}-rotational echo adiabatic passage double resonance (REAPDOR) or ^{27}Al{^{7}Li}-REDOR NMR. Another class of metastable crystalline materials with outstanding (an)ion transport properties are mixed metal fluorides such as $Ba_{1-x}La_xF_{2+x}$. Known to be fast fluoride ion conductors for decades, the origin of the fast conductivity and even the microstructure of these compounds remain to be clarified. Mechanosynthesis enabled the preparation of $Ba_{1-x}La_xF_{2+x}$ over the whole range of compositions which allowed new insights into the structural evolution of these compounds going from the fluorite structure of the BaF_2 to the tysonite structured LaF_3. Furthermore, we investigated the synthesis of $SrMgF_4$, which turned out to be accessible via high-energy ball milling. Although XRD studies help to follow the

global structural evolution, ^{19}F-MAS NMR spectroscopy may offer further insights into the evolution of the microstructure with composition, allowing for an identification of the various fluorine coordination spheres $FM_{4-x}M'_x$. First steps were done in the investigation of the structure of a new polymorph of SnF_2. Its high lability impeded the use of other techniques like TEM to solve the structure of the nanosized crystallites.

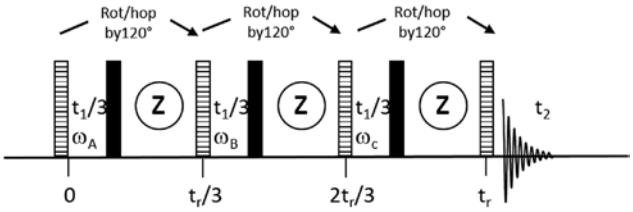

Fig. 1: Schematic representation of the principle of magic angle hopping and magic angle turning. Dashed rectangles represent 90° pulses bringing the magnetization into the xy-plane, the filled rectangles 90° pulses, which select either the sin- or the cos-component for storage along z.

Results

The organization of this section is as follows. The first part is devoted to novel NMR methods, specifically novel dipolar based magic angle turning techniques (Section "Development of dipolar NMR spectroscopy without fast magic angle spinning") and the realization of high temperatures for in situ measurements employing inductive heating (Section "Towards high-temperature high speed MAS"). Subsequently, results from the application of NMR approaches to two selected projects from within the priority program will be reported.

Specifically, the study of the crystallization of LAGP, one of the most promising crystalline solid electrolytes for application in Li batteries, from a glass matrix and the characterization of the resulting phases will be addressed in Section "Crystallization of LAGP from amorphous aluminogermanophosphate glasses". Finally, in the Section "NMR investigations of metastable fluorides", the synthesis and characterization of complex metal fluorides will be reported.

Development of dipolar NMR spectroscopy without fast magic angle spinning

As outlined in the introduction, the development of an NMR methodology which would allow to obtain structural information on short (1–2 Å) and intermediates (2–8 Å) length scales without having to resort to a fast sample spinning marked one of the central goals of the project. In principle, the high resolution which can be obtained under the conditions of fast MAS is also achievable when correlating the magnetization from a sample which is under the magic angle at three different rotor positions which are separated by 120° [64, 65]. Figure 1 illustrates the principle of this process, which may be realized either by discrete hops between the three positions (magic angle hopping) [64, 65] or by continuous sample rotation (magic angle turning) [66]. It is important to note that these rotation frequencies are in the range of 0–100 Hz, thus the generated g-forces are several orders of magnitude lower than in conventional MAS NMR experiments. Only one component, either the sin- or the cos-component is stored in the z-direction via the storage pulses (filled rectangles in Figure 1). Then, a 2D Fourier transformation produces a two-dimensional spectrum in which the full chemical shift information is retained in the direct dimension (F_2), whereas the indirect dimension only contains the isotropic parts of the chemical shift tensor.

The magic angle hopping version, introduced by Bax in 1983 [64], may suffer from imprecise positioning of the sample; the development of the continuous rotation method (at spinning speeds of 0–100 Hz) as introduced by Gan in 1992 [66] marks a considerable progress. The continuous slow rotation is easier to achieve and maintain throughout the course of the experiment, today most state of the art NMR probes can be set to slow spinning speeds and are suitable for MAT experiments, even though some restrictions still apply.

Especially under the very low speeds (100 Hz and less) applied, small variations in the rotation frequency may severely affect the resulting spectrum. This is shown in Figure 2, in which hypothetical MAT spectra of a I = ½ nucleus exhibiting exclusively CSA interaction ($\delta_{iso} = 2$ ppm, $\delta_{CSA} = 112$ ppm, $\eta_{CSA} = 0$, $B_0 = 9.4$ T) at a MAT frequency of 30 Hz are plotted as a function of the rotor frequency mismatch. As variations of this magnitude are very normal for the conventional air-driven spinners as implemented in all commercially available MAS probes we decided to resort to a mechanical, gear-driven rotation. The probe has been designed to provide stable rotation in the range of 1–100 Hz, facile setting of the magic angle and a double resonance layout of the resonance circuit to allow for dipolar based experiments. Further, the probe design has been intended to allow for further modifications such as, e.g. sample heating.

Hardware: In the MAT probe prototype developed during this project the electromotor which accomplishes

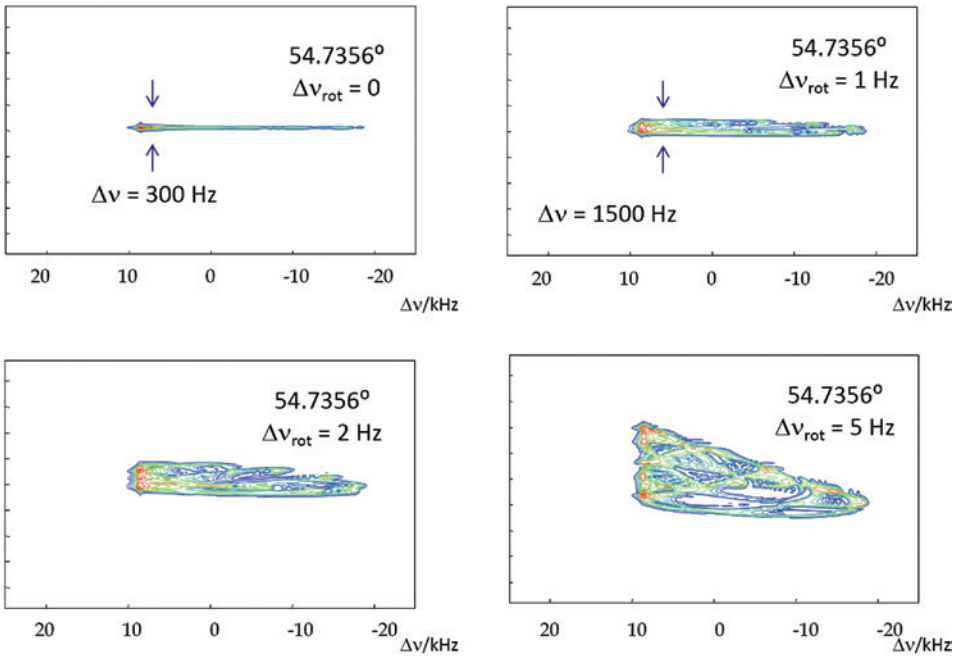

Fig. 2: Effect of a deviation from the set rotor frequency for the indicated values. Even for deviations as small as 1–2 Hz the pulse sequence runs out of synchrony entailing a drastic broadening of the projections onto the vertical (F_1) axis.

the sample rotation (via a set of gears and bevel gears) had to be positioned outside the stray field of the magnet.

The implemented electric step motor (SANYO Electric Stepsyn 242H) provides step sizes of 0.225°, 0.45°, 0.9° and 1.8°, generating sufficient torque to allow to multiply the speed via a set of gears. In the setup, a 1:3 (at the motor) and a 1:2 transmission ratio (in the tubular part of the probe) were applied, resulting in a six-fold increase of the rotation frequency. This allows the usage of the smaller step size, resulting in a smooth rotation during the experiment. An experimental setup with purely gear-driven sample containers has been reported by Bax [64], however, with the electromotor of the ensemble placed on top of the magnet, which impedes a quick installation and removal of the complete MAT probe.

The motor and the driving electronics (SANYO Electric PMM-MD-23220-21) are mounted in an aluminum casing on one end, where the tubular part of the probe arises from the other end. The tubular part is supported by a brazen pillar and houses the circuit electronics and the Hall probe for the adjustment of the magic angle. To be able to adjust the magic angle, two bevel gears are used near the sample container (cf. Figure 3). These two gears do not mesh together as flawlessly as the remaining gears do, thus under heavy duty some abrasion of brass was observed. A second bearing had to be secured to the rod meshing with the angled bevel gear to reduce abrasion due to jittering. It should be noted that our setup principally allows magic angle hopping, however, magic angle turning is far less demanding for the hardware.

While all gears were made from brass, the bevel gear at the lower end of the rotor had to be manufactured from polyoxymethylene to avoid heating effects.

To aid in the setting of the magic angle, a Hall probe, as implemented by Levitt and coworkers [67], is incorporated in the angle-adjustable part of the probe. The Hall probe (LakeShore HGCT 3020) is controlled via an in-house built assembly, allowing different supply currents from 1 to 300 mA (100 mA were typically used) and resulted in Hall voltages in the range of ± 300 mV. As all four wires leading to the Hall probe in the top of the probe act as antennas when used, the Hall probe should be disconnected after the initial setup of the magic angle.

The motor was controlled via LabVIEW routine, which was run on an external computer equipped with a National Instruments PCI 6221 card and connected to the National Instruments BNC 2121 connector block.

To allow for dipolar based NMR experiments, the resonance circuit (cf. Figure 4) was designed as a double resonance circuit.

Testing the MAT probe: The functionality of the MAT probe was tested employing a binary phosphate glass $55K_2O–45P_2O_5$ as a test sample, which was doped with small amounts of $MnCO_3$ to shorten the T_1 relaxation of ^{31}P. For this glass composition we expect the presence of two distinct ^{31}P NMR signals from two different network

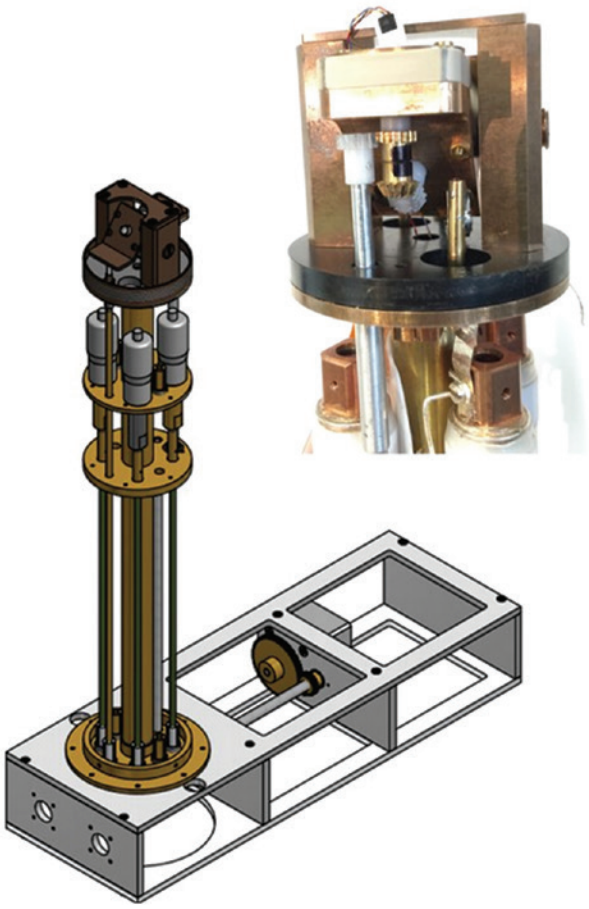

Fig. 3: Prototype MAT probe for dipolar based NMR experiments: The electromotor is located at the lower right end side of the L-shaped assembly. Employing a set of gears, the rotation is transferred to the sample container (see insert).

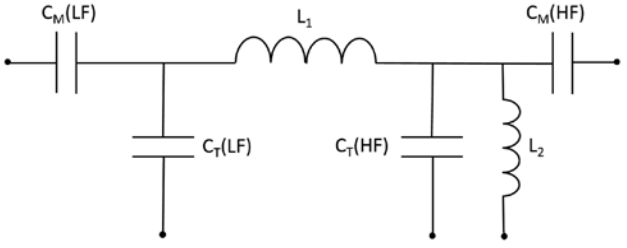

Fig. 4: Resonance circuit of the MAT probe: C_M(LF) and C_M(HF) are the matching capacitors for the high frequency (80–180 MHz) and low frequency (33–63 MHz) side of the circuit, C_T(LF) and C_T(HF) the corresponding tuning capacitors. All capacitors cover a range of 1.5–52 pF. The coils L_1 (4 turns, ∅ 7 mm) and L_2 (2.5 turns, ∅ 7 mm) are made from a silver-coated copper wire with L_1 being the measuring coil.

polyhedra [59], Q^1 (chain end) units at –5 ppm and Q^2 (chain) units at –20 ppm. A variety of different pulse sequences have been designed for the implementation of the MAT principle. Whereas the original sequences developed by Bax and Gan as well as the PHORMAT (PHase cORrected MAT) [68] experiment rely on projecting the magnetization back and forth from the z-direction, in the FIREMAT (FIve π REplicated MAT) [69] approach the magnetization is kept in the xy-plane.

In the current implementation, only two projections of the magnetization onto z were used (cf. Figure 5), as this approach retains the highest fraction of magnetization [64, 66]. The detection commences immediately following the fifth pulse, thus recording the full echo and entailing a spectrum which has to be sheared. Figure 6 collects the unsheared and sheared 2D ^{31}P MAT spectrum of the $55K_2O$–$45P_2O_5$ glass, obtained at a rotation frequency of 33.3 Hz. In the projection of the 2D spectrum onto the F1 axis the two signals from Q^1 and Q^2 phosphate groups are clearly resolved. Thus, even for amorphous phosphate samples with their inherent distribution of chemical shifts the signals can be clearly resolved, even at a spinning speed of 33.3 Hz.

Although the S/N ratio achievable with the home-built MAT probe seems to be a bit limited, with the spectrum presented the functionality of the MAT probe has been successfully proved, thus principally allowing to obtain high resolution isotropic chemical shift information without the need to apply fast MAS. However, as the final completion of the probe has been achieved just shortly before the end of the priority program, the dipolar based MAT experiments were developed and tested employing a

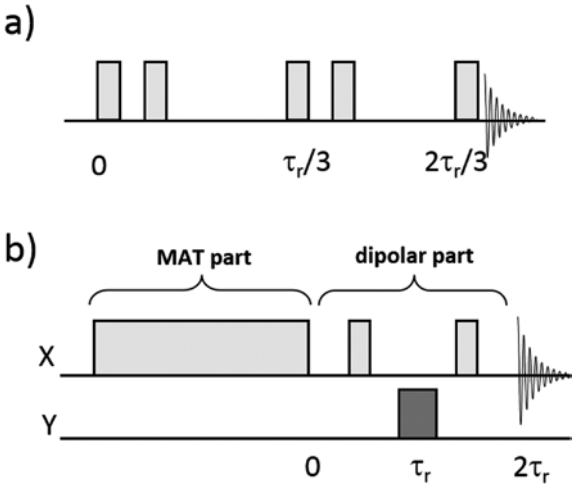

Fig. 5: Schematic representation of MAT and dipolar MAT pulse sequences used in this work: (a) five pulse MAT as introduced by Gan et al., (b) dipolar MAT: The MAT block is followed by a two cycle REAPDOR sequence. The pulses within the dipolar block are π-pulses (X channel) and a $\tau_r/3$ pulse (Y-channel, with τ_r denoting the MAT period). Setting the pulse power of the dark grey pulse on the Y-channel to 0 W constitutes the reference experiment.

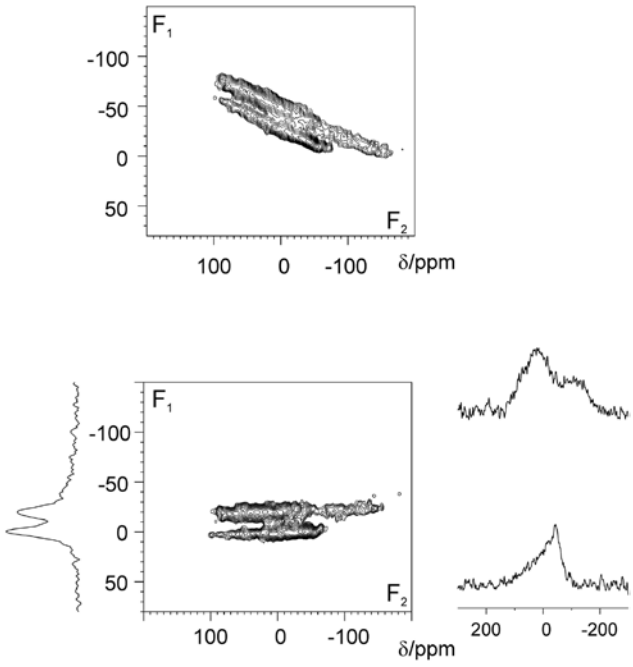

Fig. 6: Unsheared (top) and sheared (bottom) ^{31}P MAT NMR spectrum of the $55K_2O–45P_2O_5$ glass sample. The two one dimensional spectra right to the sheared spectrum represent slices at the identified isotropic positions of 0 ppm and –20 ppm, which resemble the CSA tensors of the phosphate Q^2 and Q^1 groups present in the sample. In the projection onto the F_1 axis the two signals are clearly resolved.

conventional 4 mm MAS NMR probe from Bruker, in combination with a Bruker NMR RockSolid unit which allows stable spinning speeds as low as 30 Hz.

As the results of the implementation of dipolar based NMR approaches into the MAT approach have been described in detail in a previous publication, only the salient features are repeated here. For more details the reader is referred to ref. [59].

As a test sample for the dipolar based MAT NMR experiments a ternary aluminophosphate glass $55K_2O–5Al_2O_3–40P_2O_5$ was chosen. In addition to the signals for the Q^2 and Q^1 units in this glass a further component at –8 ppm can be observed, which originates in Q^1_{1Al} units, i.e. a phosphate tetrahedron bridged via oxygen to one further phosphate tetrahedron and to one AlO_6 polyhedron. The dipolar coupling between ^{27}Al and ^{31}P nuclei may be evaluated simply by replacing the final $\pi/2$ pulse of the MAT sequence by a two cycle REAPDOR fragment (cf. Figure 5). Then, the intensity of the signals from phosphate polyhedra with connection to aluminate polyhedra should decrease with increasing ^{27}Al pulse power.

We note that we had to adjust the spinning speed to 400–670 Hz to overcome the T_2^* signal loss, which however still represents quasistatic conditions for the ^{31}P resonances [59]. In the ^{31}P MAT spin echo spectrum (cf. Figure 7 left) the three signals at 0 ppm (Q^1), –8 ppm (Q^1_{1Al}) and –18 ppm (Q^2) can be clearly identified in good agreement with the data obtained from fast MAS experiments, in the ^{31}P{^{27}Al}-MAT-REAPDOR-NMR spectrum (cf. Figure 7) the –8 ppm signal from the (Q^1_{1Al}) unit is almost completely absent, asserting that qualitative dipolar information is indeed accessible even without fast MAS.

Upon varying the ^{27}Al RF amplitude the intensity of the –8 ppm signal decreases with increasing RF power, which may principally be used to extend this approach to a quantitative evaluation of the coupling strength.

Apart from REDOR and its variants, cross polarization techniques with magnetization transfer from a nucleus X to a nucleus Y represent a further dipolar based NMR method

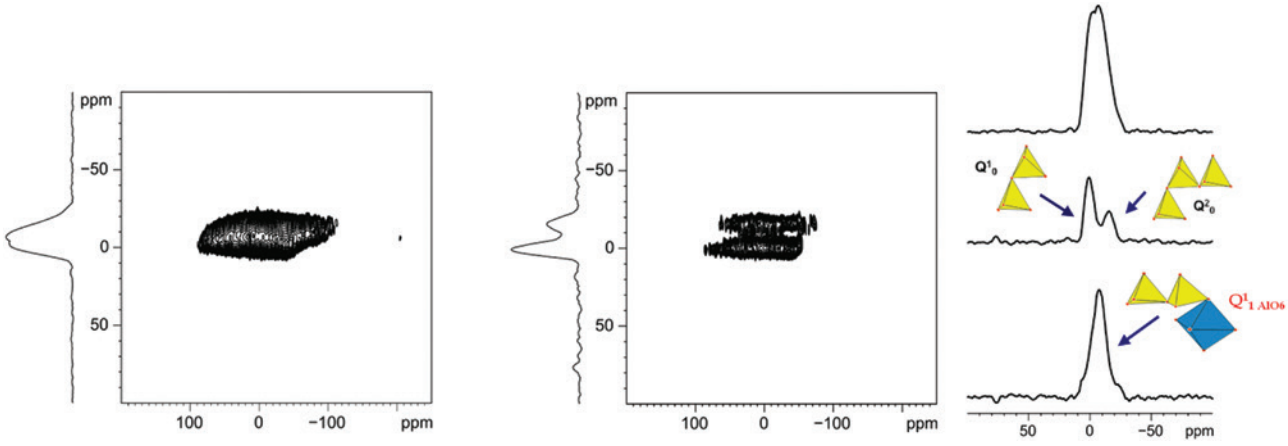

Fig. 7: ^{31}P{^{27}Al}-REAPDOR-MAT-NMR-spectroscopy for the ternary $55K_2O–5Al_2O_3–40P_2O_5$ glass: left: ^{31}P MAT spin echo NMR (no ^{27}Al-irradiation); middle: ^{31}P-{^{27}Al}-REAPDOR-MAT NMR (^{27}Al-pulse: 100 W; 500 μs); right: projections of the ^{31}P MAT spin echo NMR (top) and ^{31}P{^{27}Al}-REAPDOR-MAT NMR spectra (middle) onto the vertical (F_1) axis and the difference of the two spectra (bottom). Adapted from ref. [59] with permission from Elsevier.

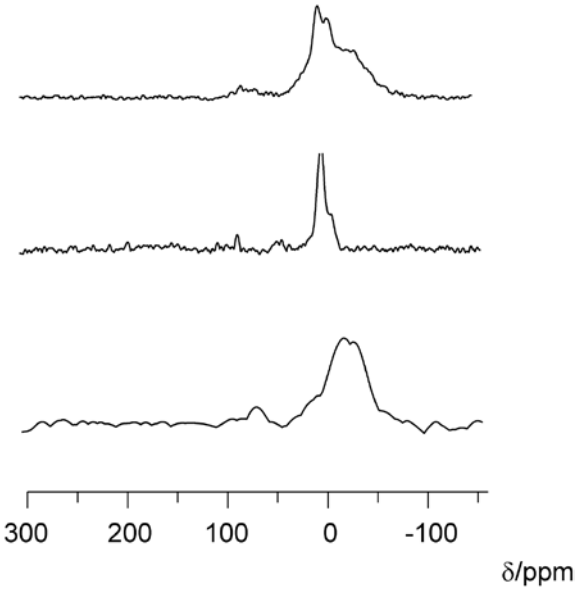

Fig. 8: Projections onto the vertical (F_1) axis from a ^{31}P-MAT-NMR-(top), ^{31}P{^{1}H}-CP-MAT-NMR (middle) and ^{31}P{^{27}Al}-CP-MAT-NMR (bottom), obtained on a mixture of a non-annealed sodium phosphate gel and a sodium aluminophosphate glass. (adapted from ref. [59]) with permission from Elsevier.

which allows to obtain qualitative information about the connectivity motifs present. This has been successfully tested with ^{31}P{^{1}H}-CP-MAT NMR and ^{31}P{^{27}Al}-CP-MAT NMR spectroscopy on a mixture of a sodium metaphosphate gel and a $26NaPO_3$–$74Al(PO_3)_3$ glass (cf. Figure 8) [59].

In the ^{31}P-MAT NMR experiment three signals may be identified and assigned to $P(OAl)_2O$- (–32 ppm), $P(OH)_2O_2$- (2 ppm) and $P(OH)O_3$-environments (–6 ppm). Here, CP was used as a dipolar filter. In the ^{31}P{^{1}H}CP-MAT NMR experiment (middle slice in Figure 8) exclusively the signals of the phosphate species at 2 ppm and –6 ppm (both with P–O–H bonds) are excited, whereas in the ^{31}P{^{27}Al}-CP-MAT NMR experiment only the signal at –32 ppm (P-O-Al units) is visible in the vertical (F_1) projection. The experiments were performed at a rotation frequency of 30 Hz.

Thus, the described experiments illustrate that MAT experiments may be employed to obtain structural information on short (1–2 Å; via the evaluation of the isotropic chemical shifts) and intermediate (2–6 Å; via an exploration of the dipolar couplings) length scales without the need for fast MAS.

Towards high-temperature high speed MAS NMR

MAS NMR experiments at high temperatures still present an experimentally rather challenging task. While for the temperature range up to 300 °C probes are commercially available which allow rotation frequencies of up to 10 kHz, experiments at higher temperatures require specialized hardware. Two commercial systems are available: The LASER MAS system from Bruker Biospin relies on heating the sample with a laser beam from a diode laser which is fed through an optical fiber until close to the sample. The system from Doty Sci. relies on conventional heating with hot nitrogen gas. The operation of both systems is far from routine and needs special expertise. Although both systems allow the application of MAS NMR at temperatures of up to 700 °C, the maximum achievable rotation frequency of 4000 Hz (Bruker) and 5500 Hz (Doty) represents a serious drawback and limits the applicability of these systems. An alternative heating approach utilizes inductive heating [70–72], using, e.g. the proton channel of a commercial MAS probe to inductively heat the sample. Here we report that by using rotor inserts machined from boron nitride (cf. Figure 9), which are coated with a thin metal layer, this method makes high temperature experiments at high spinning speeds in an unmodified standard NMR-Probe (for the experiments here standard Bruker 4 mm MAS probes were employed) possible, even without an external heating system. We developed a combined vapor deposition/galvanization process to coat the inserts and used different metals

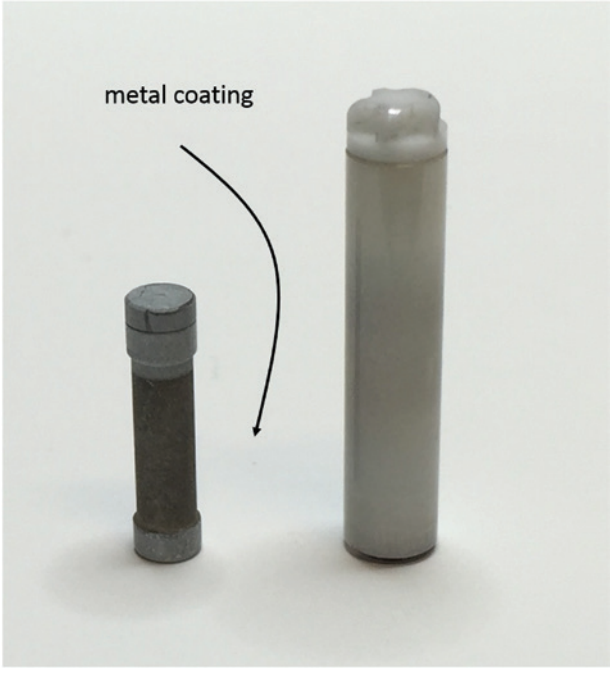

Fig. 9: Insert (left), manufactured from boron nitride for a Bruker 4 mm spinner (right). The arrow marks the part of the insert which is coated with platinum or silver.

including platinum, gold and silver to fabricate the coatings. Details of the coating process are given elsewhere [73]. For the experiment we used the 300 MHz ^{1}H channel of a Bruker double or triple resonance probe. The low power output of the SGU (signal generation unit) was connected to an external amplifier which is optimized for continuous wave (cw) operation. Heating was then performed using the electrical component of the ^{1}H RF, either under cw decoupling or using a decoupling sequence in which decoupling pulses of variable length are separated by variable periods in which no RF power is applied to the ^{1}H channel.

In a typical experiment, the data acquisition was preceded by cw-irradiation for 2–5 min to ensure temperature equilibration. We found that equilibration usually was reached after just 2 min of cw-irradiation. To check the performance of this heating approach we used the ^{79}Br resonance of KBr, which has been established as a reliable chemical shift thermometer.

Figure 10 (top) shows the obtained temperatures as a function of the cw-irradiation power for a typical insert. The rotor frequency was set to 9.5 kHz. The observed S/N ratio was found to be very acceptable in view of the losses as described in Ref. [73]. In addition we found that the line width of the ^{79}Br resonance did not increase as compared to the measurement at room temperature suggesting a rather moderate temperature gradient. Thus, with this setup we are able to heat the samples to temperatures of up to 700 °C at spinning speed of > 9 kHz. This can be considered a significant advancement in high-temperature MAS NMR. Inserts having been coated following the same coating procedure have been found to exhibit the same heating performance, thus allowing to fabricate inserts with specified heating performance in larger quantities.

As an example in Figure 10 (bottom) the ^{31}P-MAS NMR spectra of a binary potassium phosphate glass are reproduced as a function of temperature. For this glass, fast exchange between the two different local phosphate polyhedra Q^3 and Q^2 is observed at $T > 670$ K (for more details see ref. [74]). From a comparison of the spectra obtained here at $\nu_{MAS} = 9.5$ kHz with those acquired at 5 kHz, the improvement in the resolution is obvious (cf. Ref. [74]).

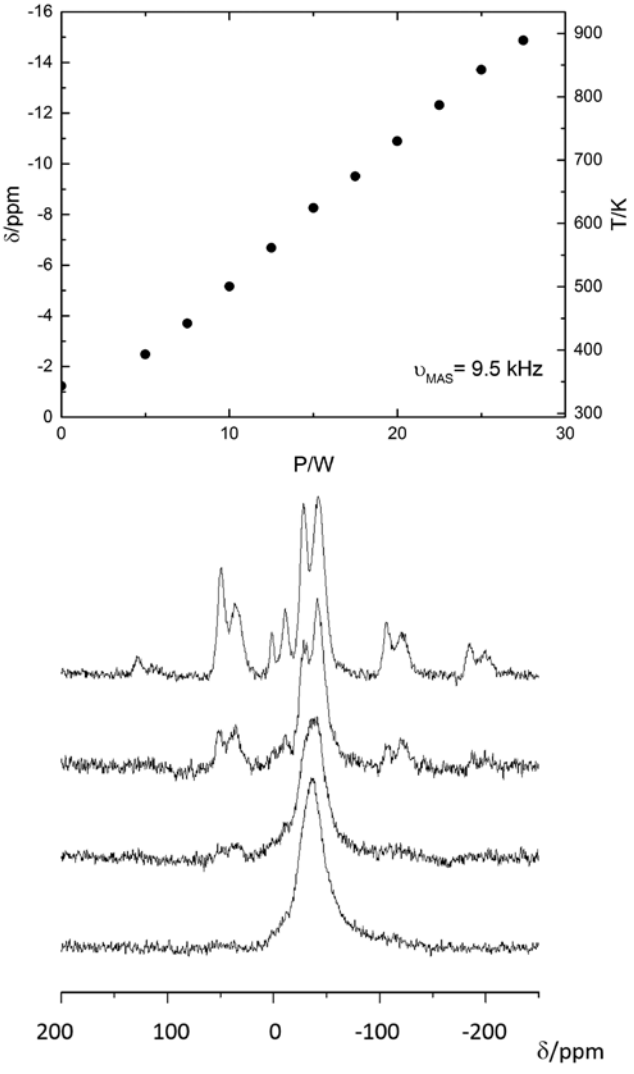

Fig. 10: Top: Chemical shift position of the ^{79}Br line (left) and temperature (right) as a function of the cw-irradiation power. MAS was performed at 9.5 kHz. Bottom: ^{31}P-MAS NMR spectra of a $20K_2O–80P_2O_5$ glass as a function of temperature (from top to bottom: 334 K, 605 K, 649 K, 778 K). Adapted from ref. [73] with permission from Elsevier.

Crystallization of LAGP from amorphous aluminogermanophosphate glasses

Fueled by the continuous quest to improve the performance of rechargeable batteries [75–80] for use in automotive transportation, research in the field of advanced battery systems marks a rather vivid field of research in the area of energy related materials. Among the various systems, Li based batteries – Li ion, Li air or Li sulfur – are considered as the most promising candidates for next generation mobile energy storage systems. Although the last decade has witnessed tremendous progress in the field, especially the usually employed liquid electrolyte poses serious issues such as environmental safety, limited temperature window and fire hazards. During the last two decades, a large variety of solid electrolytes has been studied and evaluated. For an extensive report on NMR studies (see Ref. [81]). Recent studies especially highlighted the advantageous properties of crystalline

and glass ceramics materials such as those derived, e.g. from the garnet structure $A_3B_2C_3O_{12}$ [82–86], from the family of argyrodites [87, 88] or glass ceramics such as the LAGP family [89–94] – lithium aluminum germanium phosphate, $Li_{1+x}Al_xGe_{2-x}P_3O_{12}$ glass-ceramics. Starting from the NASICON structure for pristine LGP, lithium germanophosphate, which consists of GeO_6 octahedra linked via corner-sharing to PO_4 tetrahedra with lithium cations occupying exclusively the M_1 sites, the replacement of a fraction of Ge^{4+} by Al^{3+}/Li^+ introduces additional Li^+ ions which subsequently fill the M_2 sites and Al replaces Ge. This then produces a remarkably high Li mobility with conductivity values as high as 5.08×10^{-3} S cm^{-1} at ambient temperature [94] for $Li_{1.5}Al_{0.5}Ge_{1.5}(PO_4)_3$. The preparation of these superionic crystals usually proceeds via crystallization from an amorphous precursor glass, derived either from conventional melt-quench techniques or from sol-gel processing or via high energy ball milling.

However, fine tuning of the Li conductivity requires detailed knowledge about the formation of the LAGP phase from the parent amorphous aluminogermanophosphate glasses and about the presence and nature of side phases, which usually seriously degrade the conductivity. In an attempt to unravel the crystallization mechanism of LAGP as a function of composition and temperature and to find optimum compositions and annealing profiles for the generation of materials with optimum performance, we performed an extended advanced solid state NMR study on LAGP glasses and ceramics in the compositional range $Li_{1+x}Al_xGe_{2-x}P_3O_{12}$ with $0.4 \le x \le 1.0$. The crystallization process was studied ex situ on annealed samples as well as in situ employing the inductive heating approach as outlined in Section "Towards high-temperature high speed MAS". The ex situ studies have already been published in ref. [95] and will be only briefly reproduced here. While the results of one-dimensional ^{27}Al- and ^{31}P MAS NMR experiments allow for the characterization of the local structural arrangements such as the distribution of Al within the LAGP structure, the performed ^{27}Al{^{31}P}REDOR, ^{27}Al{^{7}Li}REDOR and ^{31}P{^{27}Al}REAPDOR NMR experiments aid in the identification of more extended structural motifs.

Structure of the precursor glass matrix: For the precursor glasses of compositions $0.4 \le x \le 0.8$, the ^{31}P-MAS NMR spectra exhibit a non-resolved broad signal centered around –24 ppm. The corresponding ^{27}Al-MAS NMR spectra indicate the presence of Al in four-, five- and six-coordination by oxygen with AlO_4 units representing the dominant Al species. Employing dipolar NMR spectroscopy (data not shown) [95], the structural motifs on an extended length scale could be analyzed. With the help of an ^{31}P{^{27}Al}REAPDOR experiment on the glass $x = 0.5$ an average number of 1 P-O-Al connection per phosphorous atom is found, according to ^{27}Al{^{31}P}REDOR, AlO_4 and AlO_6 polyhedra are connected to four and five phosphate polyhedra, respectively. In addition, the presence of P-O-P connectivity was confirmed employing one-dimensional ^{31}P-refocused INADEQUATE experiments, in agreement with a DQ-DRENAR study by Eckert et al. [96] From our results we conclude the presence of $PO(OAl)(OGe)_{2-x}(OP)_x$ with $x < 1$ as the dominant extended structural motif. These are also compatible with the observed chemical

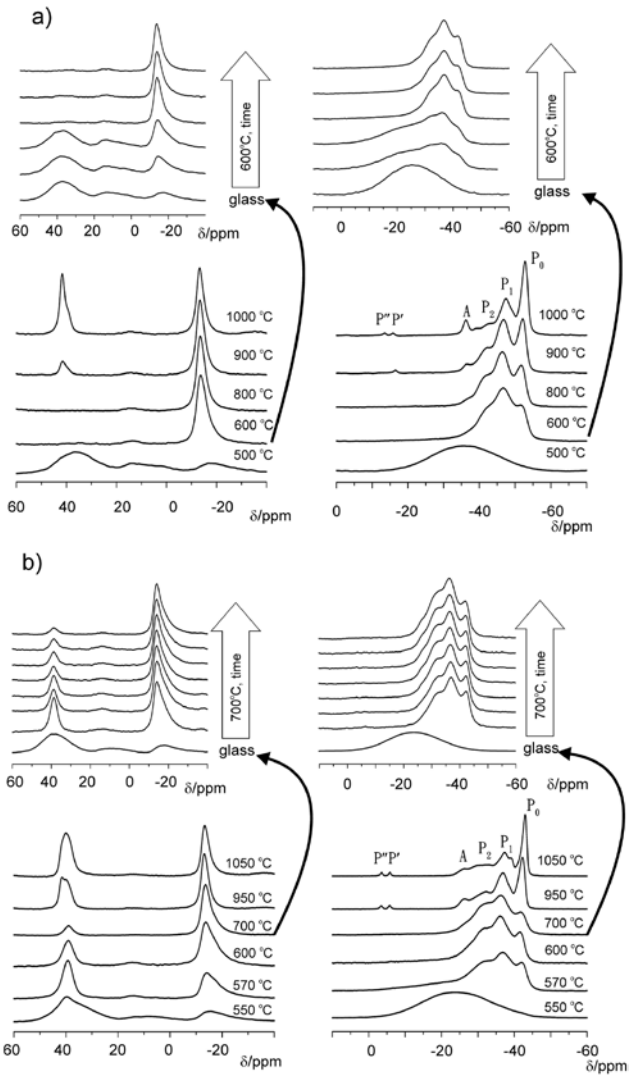

Fig. 11: Compilation of ^{27}Al- (left) and ^{31}P-MAS-NMR spectra (right) of melt-quenched $Li_{1.5}Al_{0.5}Ge_{1.5}(PO_4)_3$ (a) and $Li_{1.7}Al_{0.7}Ge_{1.3}(PO_4)_3$ (b) for the indicated annealing temperatures. Annealing times (at $T = 600$ °C) for $Li_{1.5}Al_{0.5}Ge_{1.5}(PO_4)_3$ are 30 min, 40 min, 50 min, 1 h and 3 h (from bottom to top); for $Li_{1.7}Al_{0.7}Ge_{1.3}(PO_4)_3$ the annealing times (at $T = 700$ °C) are 5 min, 30 min, 1 h, 3 h, 5 h, 7 h and 11 h. Adapted from ref. [95] with permission from Elsevier.

shift, considering the downfield shifting effect of Al and Ge as next nearest neighbor to P.

Crystallization of LAGP from the glass matrix: In Figure 11, the ^{27}Al- and ^{31}P-MAS NMR spectra for melt quench derived LAGP with $x = 0.5$ and $x = 0.7$ as a function of annealing temperature and time are given. First indication of crystalline LAGP for $x = 0.5$ is observed at $T = 600$ °C, after an annealing time of $t = 30$ min. The emerging signals at –42 ppm, –37 ppm, –32 ppm and –27 ppm can be assigned to $P(OGe)_{4-m}(OAl)_m$ units with $m = 0$, 1, 2 and 3 [96, 97].

With increasing annealing time (at $T = 600$ °C), the fraction of the amorphous part of the sample is gradually decreasing until it escapes detection after $t = 50$ min, indicating complete crystallization. The ^{27}Al-MAS NMR results corroborate these findings: In synchrony with the occurrence of the first ^{31}P-LAGP signals, the ^{27}Al-MAS-NMR spectra show a conversion of all three amorphous Al environments into a symmetric line centered at –14 ppm after $t = 40$ min, which can be assigned to AlO_6 units. From the results of a ^{27}Al{^{31}P}REDOR NMR study (data not shown, see ref. [95]), we can conclude a full connection of AlO_6 octahedra by PO_4 tetrahedra, i.e. the AlO_6 units are incorporated in the LAGP structure.

A quite different behavior is observed for the crystallization of the $x = 0.7$ sample (cf. Figure 11b). Here, together with the first precipitation of LAGP at $T = 570$ °C as seen from the ^{31}P MAS NMR, in the ^{27}Al spectra we find the emergence of a rather narrow AlO_4 signal, which consumes approximately 56% of the total ^{27}Al intensity. The intensity of the AlO_4 signal is first gradually decreasing with temperature until $T = 800$ °C, but then re-appears upon further heating to temperatures above 850 °C. When performing the annealing at constant temperatures of $T = 600$ °C and $T = 700$ °C, we find complete crystallization after 30 min for the former and after 5 min for the latter temperature. In both cases, a large fraction of the total Al signal intensity represents AlO_4 units. This fraction is then decreasing with prolonged annealing; at the same time, the ^{31}P-MAS NMR spectra indicate an increase in the signal intensity of the $P(OGe)_{4-m}(OAl)_m$ units with $m = 1$ and 2. From a ^{27}Al{^{31}P}REDOR-NMR experiment we conclude a coordination of AlO_4 by four phosphate units.

XRD measurements on melt-quench-derived $Li_{1.7}Al_{0.7}Ge_{1.3}(PO_4)_3$ ($x = 0.7$, data not shown), annealed at the indicated temperatures, offer complementary information about the crystallization process [95]. The onset temperature for crystallization can be identified as 550 °C. The dominant reflections can all be assigned to the LAGP structure. At the same time, a reflection around $2\theta = 35.2°$ is detected for the sample annealed at 560 °C. The intensity of this reflection is first decreasing until it virtually disappears at $T = 700$ °C. At temperatures above 850 °C, however, its intensity is increasing again, accompanied by a signal at 22°. These observations prove to be in perfect harmony with the results from the ^{27}Al NMR experiment, as both indicate the presence of $AlPO_4$. The most intense reflex for $AlPO_4$ is expected very close to the intense LAGP signals near 21.5° and can thus not be clearly assigned. Minor impurities such as GeO_2 and $Li_4P_2O_7$ can be observed and identified [95], the intensity of which increases at annealing temperatures higher than 800 °C. Thus, LAGP is the first crystalline product to be formed, accompanied by some disordered form of $AlPO_4$, which is then consumed upon further temperature increase. At temperatures above 800 °C, LAGP starts to decompose, indicated by the formation of the mentioned side phases. In the ^{31}P-MAS NMR spectra, the signal for the mixed $P(OAl)_{4-m}(OGe)_m$ units are decreasing, which indicates the removal of Al from the LAGP structure, in line with the observation of an increase in the amount of $AlPO_4$.

Crystallization model: From the experimental data as described above the following crystallization model is suggested. The drastic change in the chemical shift of the ^{31}P signal upon crystallization may most probably be traced back to a change from a network dominated by $PO(OAl)(OGe)_{2-x}(OP)_x$ units into the dominant structural motif of the crystalline phase: $P(OAl)_m(OGe)_{4-m}$. For low x-values LAGP is found as the only phase crystallizing; its Al content does not change notably upon further annealing, as suggested by the evolution of the ^{31}P-MAS NMR spectra. On the other hand, for $x = 0.7$, crystallization of LAGP is accompanied by the co-precipitation of $AlPO_4$, as seen from the XRD as well as the NMR results (vide supra).

With increasing annealing temperature and time, the change in the relative intensities of the ^{31}P signals for the $P(OGe)_{4-m}(OAl)_m$ units with $0 \le m \le 2$ suggests an increase in the amount of Al incorporated within the LAGP phase (cf. Figure 12 top), which originates in the initially precipitated $AlPO_4$. This assumption is corroborated by the reduction of the intensity of the corresponding AlO_4 signal in the ^{27}Al-MAS-NMR and the concomitant decrease in the intensity of the XRD reflex at $2\theta = 35.2°$.

The asymmetry and width of the ^{27}Al signal for the AlO_6 in LAGP is decreasing with increasing annealing temperature (cf. Figure 12 bottom), from which a successive ordering around the AlO_6 octahedra with increasing annealing temperature can be inferred. Annealing temperatures above 850 °C render the incorporation of Al unfavorable; as a consequence, Al is being removed from the LAGP structure (increase in the intensity of the $P(OGe)_4$ signal in ^{31}P-MAS NMR spectrum, cf. Figure 11),

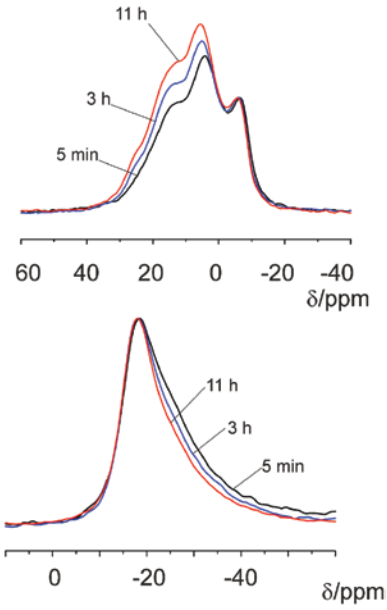

Fig. 12: Representative ^{31}P-MAS NMR (top) and ^{27}Al-MAS NMR spectra (bottom) for LAGP with $x = 0.7$, annealed at 700 °C for the indicated annealing times. Adapted from ref. [95] with permission from Elsevier.

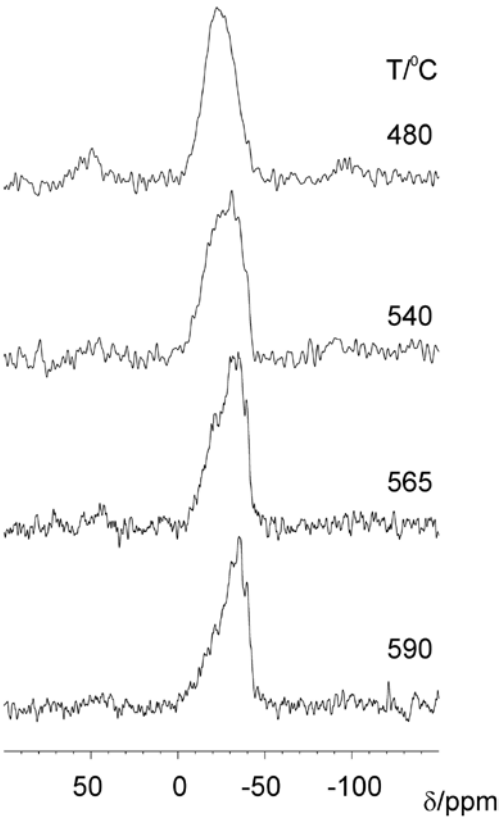

Fig. 13: In situ ^{31}P-MAS NMR spectra, obtained at a spinning speed of 8.4 kHz at the indicated temperatures. The samples were held at the temperatures for 50 min prior to data acquisition.

leading to the formation of LGP and $AlPO_4$ (increase in the corresponding ^{27}Al AlO_4 signal; observation of the XRD signals for $AlPO_4$).

In an attempt to follow the crystallization of the LAGP from the glass matrix in situ, we performed temperature dependent ^{31}P-MAS NMR experiments employing the inductive heating approach as outlined in Section "Towards high-temperature high speed MAS". Here, the rotation at frequencies > 7 kHz is necessary to clearly separate the isotropic signals from the spinning sidebands. The spectra, as collected in Figure 13, support the observations made in the ex situ experiments. Other than observed by Freude and coworkers [58], the crystallization rates for the ex situ and in situ studies seem to be comparable.

NMR investigations of metastable fluorides

In this section the results of investigations of metastable fluorides with exceptional fluoride ion conductivity are highlighted. Specifically, results on $Ba_{1-x}La_xF_{2+x}$, SnF_2 and $SrMgF_4$ will be reported.

$Ba_{1-x}La_xF_{2+x}$: $Ba_{1-x}La_xF_{2+x}$ compounds are known for exhibiting high ionic conductivity [98]. The BaF_2-LaF_3 system is characterized by a miscibility gap in the range from $x \approx 0.55$ to $x \approx 0.85$ [99, 100]. The samples with $x \leq 0.55$ were reported to crystallize in the fluorite structure in which the La ions substituting the Ba ions shall form so called 222 clusters, the ones with $x > 0.85$ crystallize in the tysonite structure [101, 102]. We investigated the possibility to close the miscibility gap by a mechanochemical synthesis approach as it was successfully done in case of the BaF_2-CaF_2 system [103].

The prepared samples showed a linear change of the lattice parameter with increasing x up to $x = 0.80$ [104]. The XRPD patterns of the samples with $0.75 \leq x \leq 0.85$, however, showed peaks which could be ascribed to both, the fluorite structure and the tysonite structure [104]. Hence, it may be a mixture of a fluorite-type and a tysonite-type phase or it might be a compound exhibiting structural properties of both structures. The linear change of the lattice parameter as a function of the composition up to $x = 0.80$ points to a complete substitution of La ions for the intended amount of Ba ions in BaF_2. To get insight into the microstructure of the compounds we performed ^{19}F-MAS NMR measurements. The ^{19}F-MAS NMR spectrum of the ball milled, nanocrystalline LaF_3 consists of two clearly separated NMR lines representing the three lattice sites of the fluoride ions: F1-sites coordinated by four La

ions, and F2 and F3 sites which are trigonally coordinated. As the F2 and F3-sites are characterized by very similar chemical environments for the fluoride ions the respective NMR lines have very similar chemical shifts, such that they overlap in case of nanocrystalline LaF_3. The ^{19}F-MAS NMR spectrum of BaF_2 consists of a single NMR line representing the tetrahedrally coordinated fluoride ions. Interestingly, the samples with compositions in the range of $0.75 \le x \le 0.85$ exhibit two NMR lines pointing to a tysonite-type structure, although the XRPD patterns clearly show the pattern of the fluorite structure for $x \le 0.80$ to be dominant. Hence, there seem to be structural motifs similar to the ones of F2 and F3-sites present in the distorted fluorite structure of $Ba_{1-x}La_xF_{2+x}$ for these large x. Moreover, the change of the chemical shift of the NMR line representing the fluoride ions in the fluorite structure and the ones on F1 sites in the tysonite structure with x was found to be linear, cf. Figure 14. Hence, the chemical environment of the fluoride ions changes continuously with x.

Furthermore, we investigated the fluoride ion mobility in $Ba_{1-x}La_xF_{2+x}$. According to the enhanced ionic motion model introduced by Wapenaar et al. [98] the high fluoride ion mobility is caused by percolating highly conducting pathways. These pathways are the interfacial regions between the La containing clusters (so-called 2:2:2 clusters) in which no fluoride ions shall be mobile and the fluorite host lattice which shall exhibit a medium fluoride ion conductivity. Static ^{19}F NMR measurements, however, showed, that in a range from $0.10 \le x \le 0.50$ all fluoride ions are mobile at temperatures larger than 453 K [104]. Hence, the whole material is highly conductive ruling out the validity of the enhanced ionic motion model in this compositional range of mechanosynthesized $Ba_{1-x}La_xF_{2+x}$.

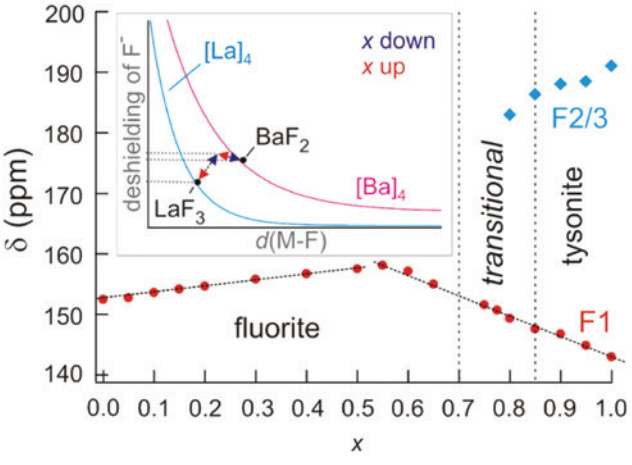

Fig. 14: Chemical shift of the maximum of the NMR lines of the spectra recorded ($\nu_0 = 565$ MHz, $\nu_{rot} = 60$ kHz) as a function of x. Figure taken from ref. [104] with permission from the American Chemical Society.

Additional measurements currently performed in our labs might elucidate the structure of $Ba_{1-x}La_xF_{2+x}$ in more detail.

SnF_2: SnF_2 crystallizes in three known structures: α-SnF_2 (monoclinic symmetry, space group $C2/c$) being the thermodynamically stable polymorph, γ-SnF_2 (orthorhombic symmetry, space group $P4_12_12_1$) forming at temperatures of about 423 K and β-SnF_2 (tetragonal symmetry, space group $P2_12_12_1$) which forms at cooling down γ-SnF_2 (transition temperature: 340 K) [105]. β-SnF_2 is known to be metastable at ambient conditions but sensitive to grinding which leads to a rapid conversion to the α-phase. In 2010 Ghedia [106] reported about a high-pressure polymorph of SnF_2 in his thesis which forms at pressures ≥ 8 GPa and temperatures ≥ 793 K. This phase could be preserved at ambient conditions but turned out to be very labile. Here we investigated the structural changes of SnF_2 due to high-energy ball milling. We milled 2 g of SnF_2 (Sigma Aldrich, 99%) in a beaker (45 mL) made of stabilized ZrO_2 equipped with 140 milling balls made of the same material (5 mm in diameter) in a Fritsch P7 premium line planetary mill at 600 rpm.

Besides a broadening of the peaks due to comminution of the crystallites and increasing lattice strain, the first clear changes of the XRPD patterns occurred after about 30 h of milling, cf. Figure 15. Most noticeable is a new peak at about 24.7° 2θ next to the peak of the stable α-SnF_2 (at 25.05° 2θ). After about 50 h of milling the XRPD pattern clearly differs from the one of α-SnF_2. Increasing the milling time to 80 h leads to further changes of the XRPD pattern. It should be noted that this change of the structure due to high-energy ball milling seems to be independent of the milling atmosphere as it can be observed after milling in air as well as in argon atmosphere. Furthermore, although these results could be reproduced, not every milling attempt led to a compound with this XRPD pattern. Sometimes almost pure α-SnF_2 was obtained after 50 h of milling, although the powder to ball mass ratio as well as the rotation speed of the mill were unchanged. The XRPD pattern cannot be matched with any of the known polymorphs of SnF_2 like β-SnF_2 and γ-SnF_2 [107, 108]. It seems plausible to assume the formation of a high-pressure polymorph of SnF_2. The XRPD pattern of the high-pressure phase of SnF_2 reported by Ghedia [106], however, differs from the one of the phase prepared within this study.

Also the XRPD patterns of other Sn_xF_y compounds or elemental Sn (which might form by a disproportionation reaction $SnF_2 \rightarrow Sn + SnF_4$) showed no agreement with the pattern of the prepared material. The change of the structure was also investigated by ^{19}F-MAS NMR spectroscopy

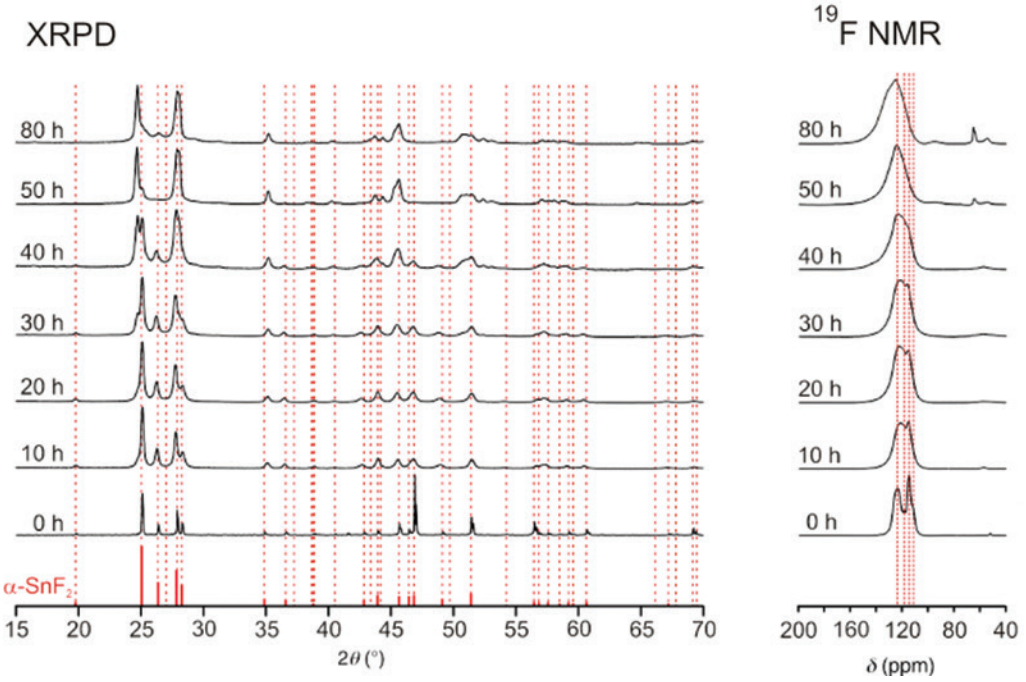

Fig. 15: Left: XRPD patterns of high-energy ball milled SnF_2 after the milling times indicated. For comparison the XRPD pattern of non-milled SnF_2 is also shown. Right: the corresponding ^{19}F MAS NMR spectra ($\nu_0 = 565$ MHz, $\nu_{rot} = 60$ kHz).

conducted with an Avance III 600 MHz spectrometer (Bruker). The measurements were done at $\nu_0(^{19}F) = 565$ MHz ($B_0 = 14.1$ T) employing a 1.3 mm MAS probe (Bruker) at a spinning rate of 60 kHz and a $\pi/2$-pulse with a duration of 1 µs (38 W). A total of 32 scans were accumulated with waiting times adjusted to be approximately $6 \times T_1$ to obtain fully relaxed spectra. The NMR lines were referenced to C_6F_6. The NMR spectrum of the non-milled α-SnF_2 reveals four NMR lines with the chemical shifts 112 ppm, 115 ppm, 119 ppm and 124 ppm which can be assigned to the four different sites of the fluoride ions in the α-SnF_2 structure [109]. The ^{19}F-MAS NMR spectrum is similar to the one reported by Bräuniger et al. [110] for α-SnF_2 although they were not able to resolve four but merely two NMR lines located at 112 ppm and 121 ppm albeit they also used a spinning rate of 60 kHz. This difference is probably due to the smaller field-strength of the magnet they used ($B_0 = 9.4$ T) for their measurements. They observed a narrow NMR line with a chemical shift of 50 ppm which they ascribed to an impurity. This NMR line is also visible in our spectra. The intensity of this line increased after the unmilled SnF_2 was stored under air for several months. Thus, it might be caused by a reaction product of SnF_2 with moisture. After milling for 10 h of SnF_2 the NMR lines start to coalesce, eventually forming a single, broad NMR line in the spectra of the SnF_2 milled for 50 h, being located at about 125 ppm.

This chemical shift is similar to the largest chemical shift in the ^{19}F NMR spectrum of the non-milled α-SnF_2. Furthermore, an additional narrow NMR line emerges at about 65 ppm. Increasing the milling time to 80 h the intensity of the narrow NMR line is increased and the broad NMR line exhibits a shoulder indicating an additional NMR line at about 130 ppm. The shift of the line to larger chemical shift values points to decreased distances between the cations and the fluoride ions, thus, a high-pressure polymorph. This is in agreement with TEM measurements which showed an increase of the crystallite volume due to the retransformation towards the α-phase which was initiated by the electron beam [D. Wang, KIT, private communication]. The high lability of the polymorph impeded electron diffraction studies on the material to elucidate the crystal structure as well as the growth of larger crystals. A comparison with the ^{19}F-MAS NMR spectrum of SnF_4 clearly shows that there is no SnF_4 present in the milled SnF_2 samples, cf. Figure 16.

If the sample milled for 50 h is stored for some weeks, its XRPD pattern changes back to the one of α-SnF_2, cf. Figure 17. Hence, the formation of oxides or oxyfluorides causing the changes in the XRPD patterns and ^{19}F-MAS NMR spectra seems very unlikely. Storage under air and storage in argon atmosphere led to very similar results. Thus, the decomposition is probably thermally induced rather than due to moisture or oxygen. Additional investigations (NMR, scattering and modeling of potential structures) to elucidate the structure of the yet unknown polymorph are currently in progress.

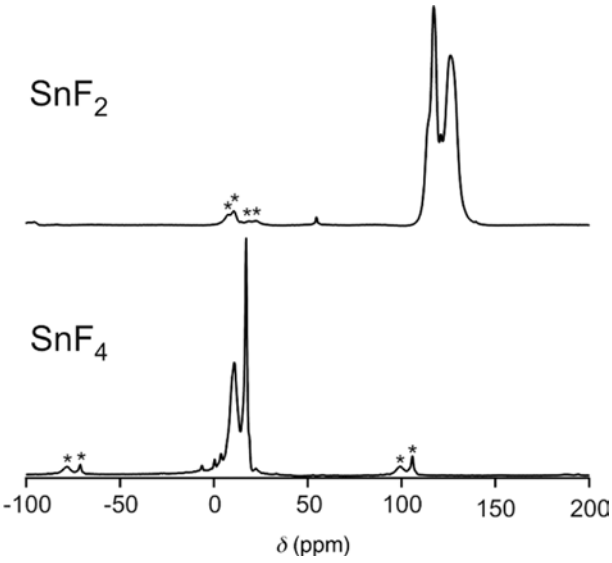

Fig. 16: ^{19}F-MAS NMR spectra of SnF_2 ($\nu_0 = 565$ MHz, $\nu_{rot} = 60$ kHz) and SnF_4 ($\nu_0 = 565$ MHz, $\nu_{rot} = 50$ kHz).

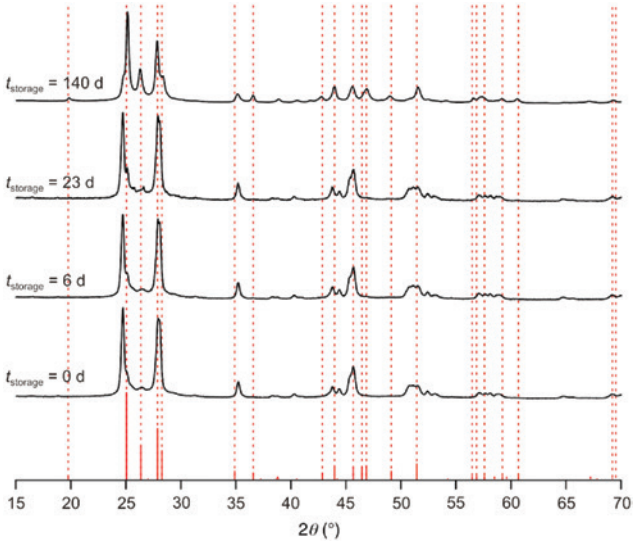

Fig. 17: XRPD patterns of the sample milled for 50 h after storage in an argon filled glovebox. The storage times are given in the figure.

$SrMgF_4$: The synthesis of $SrMgF_4$ was first reported by Banks et al. [111] in 1980 who prepared it by annealing a mixture of MgF_2 and SrF_2 in a graphite crucible three times in a row for 5 h at 1148 K. This ferroelectric material was found to crystallize in an orthorhombic structure (space group *Cmcm*) by Bingyi and Banks [112] two years later. However, in 2001 Ishizawa et al. [113] prepared a Ce^{3+} doped $SrMgF_4$ single crystal and found a much more complex monoclinic structure (space group $P112_1$) with 22 different sites for the fluoride ions. They determined the Sr:Ce ratio to be 0.9994:0.0006 and, thus, the influence of Ce^{3+} on the structure to be negligible. In 2008 a solution chemical route for the preparation was introduced by Veitsch et al. [114] Their XRPD patterns exhibited phase pure crystalline $SrMgF_4$ after annealing at 723 K for 30 min or after 3 h at 673 K. Unexpectedly, they observed a partial decomposition of $SrMgF_4$ to the binary fluorides at 773 K. Treatment at 1073 K for 4 h lead to a complete decomposition. This is in contradiction to the results obtained by Banks et al. [111] who observed incongruent melting of $SrMgF_4$ at temperatures of ca. 1173 K. Veitsch et al. [114] assumed that the heating rate and the grain size play a role. In 2015 a mechanochemical approach was used for the preparation of $SrMgF_4$, starting from Mg hydroxides (and acetates) and Sr acetates, by Scholz et al. [115]. They did not succeed in the preparation of phase pure $SrMgF_4$. However, an extensive analysis of the ^{19}F-MAS NMR line shapes revealed the presence of at least 18 different fluoride ion sites which is in good agreement with the structure determined by Ishizawa et al. [113]. Here we tried the mechanosynthesis of $SrMgF_4$ directly from the binary fluorides. For this purpose an equimolar mixture of dry SrF_2 (99.99%, Alfa Aesar) and MgF_2 (99.99%, Alfa Aesar) with a total mass of 2.0000(5) g was given into a milling beaker made of tungsten carbide (45 mL, Fritsch, Germany) together with 100 milling balls made of the same material (5 mm, Fritsch, Germany) and high-energy ball milled in a Fritsch Pulverisette 7 *premium line* for 24 h under argon atmosphere. The milling was performed in intervals of 15 min followed by 20 min pause for cooling down the milling beaker. XRPD patterns were recorded with an Advance D8 diffractometer (Bruker, Germany) in Bragg-Brentano geometry with a step size of 0.016° and 2.2 s waiting time at each step. The diffraction patterns were analyzed by Rietveld refinement employing the program TOPAS (Bruker, Germany). ^{19}F-MAS NMR measurements were performed with an Avance III spectrometer (Bruker, Germany) operated at 565 MHz with a 1.3 mm MAS probe (Bruker, Germany). The spinning speed was set to 60 kHz, the duration of the $\pi/2$-pulse was 1 µs (38 W). A total of 32 scans were accumulated with waiting times adjusted to be approximately $6 \times T_1$ to obtain fully relaxed spectra. The spectra are referenced against C_6F_6 with CaF_2 as a secondary reference material ($\delta_{iso} = 58.5$ ppm). Directly after high energy ball milling of the mixture, its XRPD pattern shows the most intense reflections of the product phase, $SrMgF_4$ (space group $P112_1$ [113]) besides a large amount of amorphous material, cf. Figure 18b). This is reflected by the ^{19}F MAS NMR spectrum shown in Figure 18a) exhibiting a very broad NMR line with two broad maxima. Additionally the NMR line of residual MgF_2 is visible. Increasing the milling time did not decrease the amount of residual

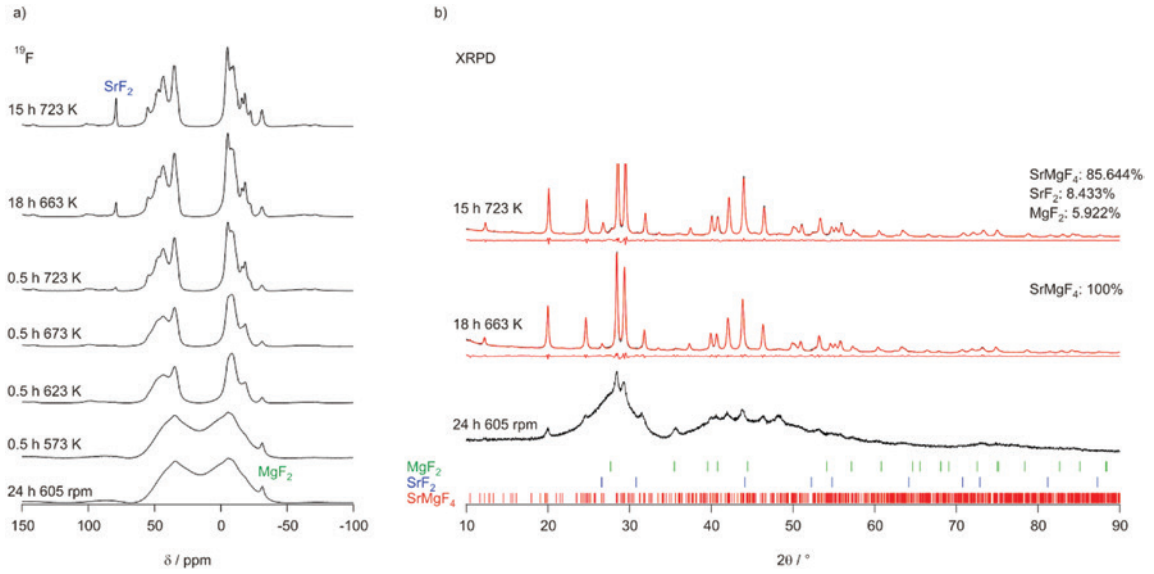

Fig. 18: (a) ^{19}F-MAS NMR spectra of a high-energy ball milled mixture of SrF_2 and MgF_2 and after heat treatment recorded at $\nu_0 = 565$ MHz and $\nu_{rot} = 60$ kHz. (b) XRPD patterns of the milled mixture and after the two long time heat treatments.

MgF_2. Also shorter milling times as well as higher or lower spinning speeds did not lead to mixtures with less MgF_2. Milling under air leads to larger amounts of MgF_2 which might be due to the presence of small traces of water [111]. However, the amount of residual educts is smaller than in the samples reported by Scholz et al. [115] which might be due to the longer milling times, the usage of a different milling vial set material or the much smaller amounts of water present in the milling beaker. Interestingly, there is no NMR line of SrF_2 in the spectrum (cf. Figure 18), although an equimolar mixture was used. In the range where its signal should show up there is a very broad line of low intensity visible. Changing the spinning speed changes the position of the maximum of this broad line but not its overall range. Thus, this line probably contains spinning side bands but probably also represents fluoride ions being situated in highly disordered Sr-rich environments. Since the chemical shift of this line is larger than the one expected for pure SrF_2 it seems likely that either d(Sr-F) is smaller than in SrF_2 (shorter d(Sr-F) values are expected for amorphous SrF_2 due to a decrease of the Madelung potential resulting from reduced long-range order) or that even larger coordination numbers than four for the fluoride ions are present.

After annealing for 30 min at 573 K the shape of the NMR line did not change. Increasing the temperature by about 50 K, however, leads to a clear change of the NMR spectrum. The maxima are now clearly separated from each other. Furthermore, the two broad lines exhibit local, narrow maxima. Further increasing the temperatures leads to an increasingly better separation of the NMR lines building up the two ranges which are most probably Mg-rich for the NMR lines situated in the range from –50 ppm to 10 ppm and Sr-rich in case of the NMR lines in the range from 25 ppm to 60 ppm (see also [115]). After 30 min at 723 K the NMR line of SrF_2 emerges. A longer temperature treatment at only 663 K shows a similar effect. The small amounts of SrF_2 and MgF_2 visible in the spectrum of this sample are not visible in the XRPD pattern. The Rietveld refinement results in 100% pure $SrMgF_4$. Of all samples prepared that exhibit a good crystallinity this one shows the lowest amount of MgF_2 and SrF_2. A temperature treatment for 15 h at 723 K leads to an increase of the amounts of SrF_2 and MgF_2 which is supported by the results of the Rietveld refinement. The presence of the educts might foster the decomposition of $SrMgF_4$. Hence, a possible cause for the decomposition of the $SrMgF_4$ samples reported by Veitsch et al. [114] at unexpectedly low temperatures might be the presence of XRPD invisible residual educts. We will try to prepare pure $SrMgF_4$ by other methods and without the presence of Ce ions in the future.

Conclusion

Recent progress in the development and application of modern NMR techniques for the characterization of crystallization processes of metastable systems from our laboratories was highlighted. With the development of an approach, in which the magic angle turning technique teams up with dipolar NMR methods such as REDOR or cross polarization we successfully introduced a

methodology to study structural motifs on short and intermediate length scales without the need of fast MAS. To ensure the most stable sample rotation as possible, rotation of the sample is accomplished via a step motor and a set of gears. The hardware layout is open and amenable to being adapted to special needs such as high temperature, etc. Further, we presented an approach to sample heating on non-spinning and spinning samples which relies on inductive heating. With this setup, stable sample spinning around $\nu_{rot} = 10$ kHz is possible for temperatures of 600 °C and higher.

For the crystallization of lithium aluminogermanophosphate, a rather promising solid electrolyte which may find application in the next generation Li batteries, we could follow the crystallization process starting from an amorphous matrix and from this develop strategies for the formation of phase pure LAGP with a high ionic conductivity. For the metal fluorides, metastable metal fluorides were synthesized via high energy ball milling and characterized via X-ray diffraction and solid state NMR techniques.

Acknowledgments: We gratefully acknowledge funding by the Deutsche Forschungsgemeinschaft within the priority programme SPP 1415. Collaborations and fruitful discussions within numerous members of the priority programme, especially with T. Nilges and M. Wiebcke are also cordially acknowledged.

References

[1] I. J. Lowe, Free induction decay of rotating solids. *Phys. Rev. Lett.* **1959**, *2*, 285.
[2] E. R. Andrew, A. Bradbury, R. G. Eades, Removal of dipolar broadening of nuclear magnetic resonance spectra of solids by specimen rotation. *Nature* **1959**, *183*, 1802.
[3] J. P. Amoureux, C. Fernandez, S. Steuernagel, Z filtering in MQMAS NMR. *J. Magn. Reson. Ser. A* **1996**, *123*, 116.
[4] L. B. Alemany, S. Steuernagel, J. P. Amoureux, R. L. Callender, A. R. Barron, Very fast MAS and MQMAS NMR studies of the spectroscopically challenging minerals kyanite and andalusite on 400, 500, and 800 MHz spectrometers. *Solid State Nucl. Magn. Reson.* **1999**, *14*, 1.
[5] C. Fernandez, J. P. Amoureux, Triple-quantum MAS-NMR of quadrupolar nuclei. *Solid State Nucl. Magn. Reson.* **1996**, *5*, 315.
[6] A. Medek, J. S. Harwood, L. Frydman, Multiple-quantum magic-angle spinning NMR: a new method for the study of quadrupolar nuclei in solids. *J. Am. Chem. Soc.* **1995**, *117*, 12779.
[7] A. Medek, L. Frydman, Multiple-quantum magic-angle spinning NMR: a new technique for probing quadrupolar nuclei in solids. *J. Braz. Chem. Soc.* **1999**, *10*, 263.
[8] Z. H. Gan, Isotropic NMR spectra of half-integer quadrupolar nuclei using satellite transitions and magic-angle spinning. *J. Am. Chem. Soc.* **2000**, *122*, 3242.
[9] K. J. Pike, S. E. Ashbrook, S. Wimperis, Two-dimensional satellite-transition MAS NMR of quadrupolar nuclei: shifted echoes, high-spin nuclei and resolution. *Chem. Phys. Lett.* **2001**, *345*, 400.
[10] S. E. Ashbrook, S. Wimperis, High-resolution NMR of quadrupolar nuclei in solids: the satellite-transition magic angle spinning (STMAS) experiment. *Prog. Nucl. Magn. Reson. Spectros.* **2004**, *45*, 53.
[11] M. J. Thrippleton, T. J. Ball, S. Steuernagel, S. E. Ashbrook, S. Wimperis, STARTMAS: a MAS-based method for acquiring isotropic NMR spectra of spin I=3/2 nuclei in real time. *Chem. Phys. Lett.* **2006**, *431*, 390.
[12] A. Goldbourt, P. K. Madhu, Multiple-Quantum Magic-Angle Spinning: High-Resolution Solid-State NMR of Half-Integer Spin Quadrupolar Nuclei, In: *Annual Reports on NMR Spectroscopy*, (Ed. G. A. Webb), Academic Press: Burlington, **2005**, vol. 54, p. 81.
[13] R. Dupree, D. Holland, P. W. McMillan, R. F. Pettifer, The structure of soda silica glasses – A MAS NMR study. *J. Non-Cryst. Solids* **1984**, *68*, 399.
[14] R. J. Kirkpatrick, MAS NMR-spectroscopy of minerals and glasses. *Rev. Miner.* **1988**, *18*, 341.
[15] R. K. Brow, R. J. Kirkpatrick, G. L. Turner, The short-range structure of sodium phosphate glasses: 1. MAS NMR studies. *J. Non-Cryst. Solids* **1990**, *116*, 39.
[16] C. A. Fyfe, Y. Feng, H. Grondey, G. T. Kokotailo, H. Gies, One-dimensional and two-dimensional high resolution solid state NMR studies of zeolite lattice structures. *Chem. Rev.* **1991**, *91*, 1525.
[17] H. Maekawa, T. Maekawa, K. Kawamura, T. Yokokawa, The structural groups of alkali silicate glasses determined from Si-29 MAS NMR. *J. Non-Cryst. Solids* **1991**, *127*, 53.
[18] X. Y. Xue, J. F. Stebbins, M. Kanzaki, P. F. McMillan, B. Poe, Pressure-induced silicon coordination and tetrahedral structural-changes in alkali oxide-silica melts up to 12 Gpa – NMR, Raman, and infrared-spectroscopy. *Am. Miner.* **1991**, *76*, 8.
[19] H. Eckert, Structural characterization of noncrystalline solids and glasses using solid-state NMR. *Prog. Nucl. Magn. Reson. Spectros.* **1992**, *24*, 159.
[20] B. Zibrowius, E. Loffler, M. Hunger, Multinuclear MAS NMR and IR spectroscopic study of silicon incorporation into SAPO-5, SAPO-31, and SAPO-34 molecular sieves. *Zeolites* **1992**, *12*, 167.
[21] R. K. Brow, R. J. Kirkpatrick, G. L. Turner, Nature of alumina in phosphate glasses. 2. Structure of sodium aluminophosphate glass. *J. Am. Ceram. Soc.* **1993**, *76*, 919.
[22] E. Brunner, Solid State NMR – A powerful tool for the investigation of surface hydroxyl groups in zeolites and their interactions with adsorbed probe molecules. *J. Mol. Struct.* **1995**, *355*, 61.
[23] C. Fernandez, J. P. Amoureux, J. M. Chezeau, L. Delmotte, H. Kessler, Al-27 MAS NMR characterization of AlPO4-14 enhanced resolution and information by MQMAS. *Micropor. Mater.* **1996**, *6*, 331.
[24] P. J. Dirken, S. C. Kohn, M. E. Smith, E. R. H. vanEck, Complete resolution of Si-O-Si and Si-O-Al fragments in an aluminosilicate glass by O-17 multiple quantum magic angle spinning NMR spectroscopy. *Chem. Phys. Lett.* **1997**, *266*, 568.
[25] M. Hunger, Bronsted acid sites in zeolites characterized by multinuclear solid-state NMR spectroscopy. *Catal. Rev.* **1997**, *39*, 345.
[26] R. K. Brow, Review: the structure of simple phosphate glasses. *J. Non-Cryst. Solids* **2000**, *263*, 1.

[27] S. K. Lee, J. F. Stebbins, Al-O-Al and Si-O-Si sites in framework aluminosilicate glasses with Si/Al=1: quantification of framework disorder. *J. Non-Cryst. Solids* **2000**, *270*, 260.
[28] H. O. Pastore, S. Coluccia, L. Marchese, Porous aluminophosphates: from molecular sieves to designed acid catalysts. *Ann. Rev. Mater. Res.* **2005**, *35*, 351.
[29] D. R. Neuville, L. Cormier, D. Massiot, Al coordination and speciation in calcium aluminosilicate glasses: effects of composition determined by Al-27 MQ-MAS NMR and Raman spectroscopy. *Chem. Geol.* **2006**, *229*, 173.
[30] G. N. Greaves, S. Sen, Inorganic glasses, glass-forming liquids and amorphizing solids. *Adv. Phys.* **2007**, *56*, 1.
[31] M. Geppi, S. Borsacchi, G. Mollica, C. A. Veracini, Applications of solid-state NMR to the study of organic/inorganic multicomponent materials. *Appl. Spectrosc. Rev.* **2009**, *44*, 1.
[32] R. Born, M. Feike, C. Jäger, H. W. Spiess, 2D P-31 Exchange NMR – a new approach for a direct probing of the connectivities of Q(N) units in glasses. *Z. Naturfors. Sect. A-J. Phys. Sci.* **1995**, *50*, 169.
[33] P. Hartmann, C. Jana, J. Vogel, C. Jager, P-31 MAS and 2D exchange NMR of crystalline silicon phosphates. *Chem. Phys. Lett.* **1996**, *258*, 107.
[34] A. E. Bennett, J. H. Ok, R. G. Griffin, S. Vega, Chemical shift correlation spectroscopy in rotating solids: Radio frequency-driven dipolar recoupling and longitudinal exchange. *J. Chem. Phys.* **1992**, *96*, 8624.
[35] J. M. Griffiths, R. G. Griffin, Nuclear-magnetic-resonance methods for measuring dipolar couplings in rotating solids. *Anal. Chim. Acta* **1993**, *283*, 1081.
[36] M. Feike, R. Graf, I. Schnell, C. Jäger, H. W. Spiess, Structure of crystalline phosphates from P-31 double-quantum NMR spectroscopy. *J. Am. Chem. Soc.* **1996**, *118*, 9631.
[37] R. Tycko, G. Dabbagh, Measurement of nuclear magnetic dipole-dipole couplings in magic angle spinning Nmr. *Chem. Phys. Lett.* **1990**, *173*, 461.
[38] Y. K. Lee, N. D. Kurur, M. Helmle, O. G. Johannessen, N. C. Nielsen, M. H. Levitt, Efficient dipolar recoupling in the Nmr of rotating solids – a sevenfold symmetrical radiofrequency pulse sequence. *Chem. Phys. Lett.* **1995**, *242*, 304.
[39] T. Gullion, J. Schaefer, Rotational-echo double-resonance Nmr. *J. Magn. Reson.* **1989**, *81*, 196.
[40] Y. Pan, T. Gullion, J. Schaefer, Determination of C-N internuclear distances by rotational-echo double-resonance Nmr of solids. *J. Magn. Reson.* **1990**, *90*, 330.
[41] T. Gullion, Introduction to rotational-echo, double-resonance NMR. *Concepts Magn. Reson.* **1998**, *10*, 277.
[42] T. Gullion, Detecting C-13-O-17 dipolar interactions by rotational-echo, adiabatic-passage, double-resonance NMR. *J. Magn. Reson. Ser. A* **1995**, *117*, 326.
[43] T. Gullion, Measurement of Dipolar Interactions between Spin-1/2 and quadrupolar nuclei by rotational-echo, adiabatic-passage, double-resonance NMR. *Chem. Phys. Lett.* **1995**, *246*, 325.
[44] C. P. Grey, W. S. Veeman, The detection of weak heteronuclear coupling between Spin-1 and Spin-1/2 Nuclei in MAS NMR – N-14/C-13/H-1 triple resonance experiments. *Chem. Phys. Lett.* **1992**, *192*, 379.
[45] H. Eckert, S. J. Elbers, D. Epping, M. Janssen, M. W. Kalwei, Strojek, U. Voigt, Dipolar Solid State NMR Approaches Towards Medium-Range Structure in Oxide Glasses, in Topics in Current Chemsitry 246, In: *New Techniques in Solid-State NMR* (Ed. J. Klinowski) p. 195, **2005**.
[46] L. van Wüllen, U. Müller, M. Jansen, Intermediate-range order in amorphous nitridic ceramics: lessons from modern solid-state NMR spectroscopy. *Angew. Chem.-Int. Edit.* **2000**, *39*, 2519.
[47] L. van Wüllen, M. Jansen, Random inorganic networks: a novel class of high-performance ceramics. *J. Mater. Chem.* **2001**, *11*, 223.
[48] L. van Wüllen, G. Schwering, B-11-MQMAS and Si-29-{B-11} double-resonance NMR studies on the structure of binary B2O3-SiO2 glasses. *Solid State Nucl. Magn. Reson.* **2002**, *21*, 134.
[49] L. van Wüllen, G. Tricot, S. Wegner, An advanced NMR protocol for the structural characterization of aluminophosphate glasses. *Solid State Nucl. Magn. Reson.* **2007**, *32*, 44.
[50] C. A. Fyfe, Y. Feng, H. Gies, H. Grondey, G. T. Kokotailo, Natural abundance 2-dimensional solid state Si-29 NMR: Investigations of 3-dimensional lattice connectivities in zeolite structures. *J. Am. Chem. Soc.* **1990**, *112*, 3264.
[51] C. A. Fyfe, K. C. Wongmoon, Y. Huang, H. Grondey, INEPT experiments in solid state NMR. *J. Am. Chem. Soc.* **1995**, *117*, 10397.
[52] A. Lesage, C. Auger, S. Caldarelli, L. Emsley, Determination of through-bond carbon-carbon connectivities in solid-state NMR using the INADEQUATE experiment. *J. Am. Chem. Soc.* **1997**, *119*, 7867.
[53] A. Lesage, D. Sakellariou, S. Steuernagel, L. Emsley, Carbon-proton chemical shift correlation in solid-state NMR by through-bond multiple-quantum spectroscopy. *J. Am. Chem. Soc.* **1998**, *120*, 13194.
[54] D. Franke, C. Hudalla, H. Eckert, Heteronuclear X-Y double quantum MAS NMR inorganic solids Applications for indirect detection and spectral editing of rare-spin resonances. *Solid State Nucl. Magn. Reson.* **1992**, *1*, 33.
[55] D. Massiot, F. Fayon, B. Alonso, J. Trebosc, J. P. Amoureux, Chemical bonding differences evidenced from J-coupling in solid state NMR experiments involving quadrupolar nuclei. *J. Magn. Reson.* **2003**, *164*, 160.
[56] S. P. Brown, Perez-M. Torralba, D. Sanz, R. M. Claramunt, L. Emsley, Determining hydrogen-bond strengths in the solid state by NMR: the quantitative measurement of homonuclear J couplings. *Chem. Commun.* **2002**, *38*, 1852.
[57] F. Fayon, I. J. King, R. K. Harris, J. S. O. Evans, D. Massiot, Application of the through-bond correlation NMR experiment to the characterization of crystalline and disordered phosphates. *Comptes Rendus Chimie* **2004**, *7*, 351.
[58] H. Liu, H. Ernst, D. Freude, F. Scheffler, W. Schwieger, In situ B-11 MAS NMR study of the synthesis of a boron-containing MFI type zeolite. *Microporous Mesoporous Mat.* **2002**, *54*, 319.
[59] A. Ananthanarayanan, L. van Wuellen, Achieving high resolution dipolar NMR information without fast sample spinning: combining magic angle turning with dipolar based NMR methods. *Solid State Nucl. Magn. Reson.* **2013**, *49–50*, 42.
[60] S. Springer, I. A. Baburin, T. Heinemeyer, J. G. Schiffmann, L. van Wuellen, S. Leoni, M. Wiebcke, A zeolitic imidazolate framework with conformational variety: conformational polymorphs versus frameworks with static conformational disorder. *Crystengcomm* **2016**, *18*, 2477.
[61] C. A. Schröder, I. A. Baburin, L. van Wüllen, M. Wiebcke, S. Leoni, Subtle polymorphism of zinc imidazolate frameworks: temperature-dependent ground states in the energy landscape revealed by experiment and theory. *Crystengcomm* **2013**, *15*, 4036.

[62] A. Düvel, A. Kuhn, L. Robben, M. Wilkening, P. Heitjans, Mechanosynthesis of solid electrolytes: preparation, characterization, and Li ion transport properties of garnet-type Al-doped $Li_7La_3Zr_2O_{12}$ crystallizing with cubic symmetry. *J. Phys. Chem. C* **2012**, *116*, 15192.

[63] V. Baran, L. van Wüllen, T. F. Faessler, Substitution of lithium for magnesium, zinc, and aluminum in $Li_{15}Si_4$: crystal structures, thermodynamic properties, as well as ^{6}Li and ^{7}Li NMR spectroscopy of $Li_{15}Si_4$ and $Li_{15-x}M_xSi_4$ (M=Mg, Zn, and Al). *Chem.-Eur. J.* **2016**, *22*, 6598.

[64] A. Bax, N. Z. Szeverenyi, G. E. Maciel, Correlation of isotropic shifts and chemical shift anisotropies by two-dimensional fourier-transform magic-angle hopping NMR spectroscopy. *J. Magn. Reson.* **1983**, *52*, 147.

[65] N. M. Szeverenyi, A. Bax, G. E. Maciel, Magic-angle hopping as an alternative to magic-angle spinning for solid state NMR. *J. Magn. Reson.* **1985**, *61*, 440.

[66] Z. H. Gan, High resolution chemical shift and chemical shift anisotropy correlation in solids using slow magic angle spinning. *J. Am. Chem. Soc.* **1992**, *114*, 8307.

[67] S. Mamone, A. Dorsch, O. G. Johannessen, M. V. Naik, P. K. Madhu, M. H. Levitt, A Hall effect angle detector for solid-state NMR. *J. Magn. Reson.* **2008**, *190*, 135.

[68] J. Z. Hu, W. Wang, F. Liu, M. S. Solum, D. W. Alderman, R. J. Pugmire, D. M. Grant, Magic-angle turning experiments for measuring chemical shift tensor principal values in powdered solids. *J. Magn. Reson. Ser. A* **1995**, *113*, 210.

[69] D. W. Alderman, G. McGeorge, J. Z. Hu, R. J. Pugmire, D. M. Grant, A sensitive, high resolution magic angle turning experiment for measuring chemical shift tensor principal values. *Mol. Phys.* **1998**, *95*, 1113.

[70] G. G. Maresch, R. D. Kendrick, C. S. Yannoni, High temperature NMR using inductive heating. *Rev. Sci. Instrum.* **1990**, *61*, 77.

[71] D. B. Ferguson, J. F. Haw, Transient methods for in situ NMR of reactions on solid catalysts using temperature jumps. *Anal. Chem.* **1995**, *67*, 3342.

[72] J. Rinnenthal, D. Wagner, T. Marquardsen, A. Krahn, F. Engelke, H. Schwalbe, A temperature-jump NMR probe setup using rf heating optimized for the analysis of temperature-induced biomacromolecular kinetic processes. *J. Magn. Reson.* **2015**, *251*, 84.

[73] H. Kirchhain, J. Holzinger, A. Mainka, A. Spörhase, A. Wixforth, L. van Wüllen, High-temperature MAS-NMR at high spinning speeds. *Solid State Nucl. Magn. Reson.* **2016**, *78*, 37.

[74] S. Wegner, L. van Wuellen, G. Tricot, Network dynamics and species exchange processes in aluminophosphate glasses: an in situ high temperature magic angle spinning NMR view. *J. Phys. Chem. B* **2009**, *113*, 416.

[75] M. S. Whittingham, Lithium batteries and cathode materials. *Chem. Rev.* **2004**, *104*, 4271.

[76] A. S. Arico, P. Bruce, B. Scrosati, J. M. Tarascon, W. Van Schalkwijk, Nanostructured materials for advanced energy conversion and storage devices. *Nature Materials* **2005**, *4*, 366.

[77] P. G. Bruce, B. Scrosati, J.-M. Tarascon, Nanomaterials for rechargeable lithium batteries. *Angew. Chem.-Int. Edit.* **2008**, *47*, 2930.

[78] J. B. Goodenough, Y. Kim, Challenges for rechargeable Li batteries. *Chem. Mat.* **2010**, *22*, 587.

[79] D. Bresser, S. Passerini, B. Scrosati, Recent progress and remaining challenges in sulfur-based lithium secondary batteries – a review. *Chem. Commun.* **2013**, *49*, 10545.

[80] B. C. Melot, J. M. Tarascon, Design and preparation of materials for advanced electrochemical storage. *Acc. Chem. Res.* **2013**, *46*, 1226.

[81] C. V. Chandran, P. Heitjans, Solid-state NMR studies of lithium ion dynamics across materials classes. *Ann. Rep. NMR Spectrosc.* **2016**, *89*, 1.

[82] V. Thangadurai, W. Weppner, $Li_6ALa_2Ta_2O_{12}$ (A=Sr, Ba): Novel garnet-like oxides for fast lithium ion conduction. *Adv. Funct. Mater.* **2005**, *15*, 107.

[83] L. van Wüllen, T. Echelmeyer, H.-W. Meyer, D. Wilmer, The mechanism of Li-ion transport in the garnet $Li_5La_3Nb_2O_{12}$. *Phys. Chem. Chem. Phys.* **2007**, *9*, 3298.

[84] S. Ohta, T. Kobayashi, T. Asaoka, High lithium ionic conductivity in the garnet-type oxide Li_{7-X} $La_3(Zr_{2-X}, Nb_X)O_{12}$ (X=0-2). *J. Power Sources* **2011**, *196*, 3342.

[85] H. Buschmann, J. Dölle, S. Berendts, A. Kuhn, P. Bottke, M. Wilkening, P. Heitjans, A. Senyshyn, H. Ehrenberg, A. Lotnyk, V. Duppel, L. Kienle, J. Janek, Structure and dynamics of the fast lithium ion conductor "$Li_7La_3Zr_2O_{12}$". *Phys. Chem. Chem. Phys.* **2011**, *13*, 19378.

[86] V. Thangadurai, S. Narayanan, D. Pinzaru, Garnet-type solid-state fast Li ion conductors for Li batteries: critical review. *Chem. Soc. Rev.* **2014**, *43*, 4714.

[87] H.-J. Deiseroth, S.-T. Kong, H. Eckert, J. Vannahme, C. Reiner, T. Zaiss, M. Schlosser, Li_6PS_5X: a class of crystalline Li-rich solids with an unusually high Li+ mobility. *Angew. Chem.-Int. Edit.* **2008**, *47*, 755.

[88] V. Epp, O. Guen, H.-J. Deiseroth, M. Wilkening, Highly mobile ions: low-temperature NMR directly probes extremely fast Li+ hopping in argyrodite-type Li_6PS_5Br. *J. Phys. Chem. Lett.* **2013**, *4*, 2118.

[89] H. Aono, E. Sugimoto, Y. Sadaoka, N. Imanaka, G. Adachi, Ionic conductivity of solid electrolytes based on Lithium Titanium Phosphate. *J. Electrochem. Soc.* **1990**, *137*, 1023.

[90] G. Y. Adachi, N. Imanaka, H. Aono, Fast Li-circle plus conducting ceramic electrolytes. *Adv. Mater.* **1996**, *8*, 127.

[91] M. A. Paris, J. Sanz, Structural changes in the compounds $LiM_2(IV)(PO_4)_3$ (M-IV=Ge, Ti, Sn, and Hf) as followed by P-31 and Li-7 NMR. *Phys. Rev. B* **1997**, *55*, 14270.

[92] M. Cretin, P. Fabry, Comparative study of lithium ion conductors in the system $Li_{1-x}Al_xA_{2-x}(IV)$ $(PO_4)_3$ with A(IV) = Ti or Ge and 0 <= x <= 0.7 for use as Li+ sensitive membranes. *J. Eur. Ceram. Soc.* **1999**, *19*, 2931.

[93] X. Xu, Z. Wen, X. Wu, X. Yang, Z. Gu, Lithium ion-conducting glass-ceramics of $Li_{1.5}Al_{0.5}Ge_{1.5}(PO_4)_3$–$xLi_2O$ (x=0.0-0.20) with good electrical and electrochemical properties. *J. Am. Ceram. Soc.* **2007**, *90*, 2802.

[94] J. S. Thokchom, N. Gupta, B. Kumar, Superionic conductivity in a lithium aluminum germanium phosphate glass-ceramic. *J. Electrochem. Soc.* **2008**, *155*, A915.

[95] Z. Liu, S. Venkatachalam, H. Kirchhain, L. Van Wüllen, Study of the glass-to-crystal transformation of the NASICON-type electrolyte $Li_{1+x}Al_xGe_{2-x}(PO_4)_3$. *Solid State Ionics.* **2016**, *295*, 32.

[96] C. Schröder, J. Ren, A. C. M. Rodrigues, H. Eckert, Glass-to-crystal transition in $Li_{1+x}Al_xGe_{2-x}(PO_4)_3$: structural aspects studied by solid state. *J. Phys. Chem. C* **2014**, *118*, 9400.

[97] Z. Liu, S. Venkatachalam, L. van Wüllen, Structure, phase separation and Li dynamics in sol-gel-derived $Li_{1+x}Al_xGe_{2-x}(PO_4)_3$. *Solid State Ionics.* **2015**, *276*, 47.

[98] K. E. D.Wapenaar, J. L. Vankoesveld, J. Schoonman, Conductivity enhancement in fluorite-structured $Ba_{1-x}La_xF_{2+x}$ solid solutions. *Solid State Ionics*. **1981**, *2*, 145.

[99] B. P. Sobolev, N. L. Tkachenko, Phase diagrams of BaF_2-(Y,Ln) F_3 systems. *J. Less Common Met*. **1982**, *85*, 155.

[100] S. V. Kuznetsov, P. P. Fedorov, Morphological stability of solid-liquid interface during melt crystallization of $M_{1-x}R_xF_{2+x}$ solid solutions. *Inorg. Mater.* **2008**, *44*, 1434.

[101] J. K. Kjems, N. H. Andersen, J. Schoonman, K. Clausen, Structure and dynamics of disordered solids – a neutron scattering study of $Ba_{1-x}La_xF_{2+x}$. *Phys. B* **1983**, *120*, 357.

[102] N. H. Andersen, K. N. Clausen, J. K. Kjems, J. Schoonman, A study of the disorder in heavily doped $Ba_{1-X}La_XF_{2+X}$ by neutron-scattering, ionic-conductivity and specific-heat measurements. *J. Phys. C* **1986**, *19*, 2377.

[103] A. Düvel, B. Ruprecht, P. Heitjans, M. Wilkening, Mixed alkaline-earth effect in the metastable anion conductor $Ba_{1-x}Ca_xF_2$ ($0 <= x <= 1$): correlating long-range ion transport with local structures revealed by ultrafast F-19 MAS NMR. *J. Phys. Chem. C* **2011**, *115*, 23784.

[104] A. Düvel, J. Bednarcik, V. Sepelak, P. Heitjans, Mechanosynthesis of the fast fluoride ion conductor $Ba_{1-x}La_xF_{2+x}$: from the fluorite to the tysonite structure. *J. Phys. Chem. C* **2014**, *118*, 7117.

[105] N. I. Sorokin, SnF_2-based solid electrolytes. *Inorg. Mater.* **2004**, *40*, 989.

[106] S. Ghedia, High pressure – high temperature investigations of solid oxides and fluorides. *MPI für Festkörperforschung*, Stuttgart **2010**.

[107] G. Denes, Phase-transitions and structural relationships between Ge_5F_{12}, GeF_2, SnF_2, and TeO_2. *J. Solid State Chem.* **1989**, *78*, 52.

[108] G. Denes, J. Pannetier, J. Lucas, About SnF_2 stannous fluoride. 2. Crystal structure of beta-SnF_2 and gamma-SnF_2. *J. Solid State Chem.* **1980**, *33*, 1.

[109] R. C. McDonald, H. H. Hau, K. Eriks, Crystallographic studies of Tin(II) compounds. 1. Crystal structure of tin(II)fluoride, SnF_2. *Inorg. Chem.* **1976**, *15*, 762.

[110] T. Braeuniger, S. Ghedia, M. Jansen, Covalent bonds in alpha-SnF_2 monitored by J-couplings in solid-state NMR spectra. *Z. Anorg. Allg. Chem.* **2010**, *636*, 2399.

[111] E. Banks, S. Nakajima, M. Shone, New complex fluorides $EuMgF_4$, $SmMgF_4$, $SrMgF_4$, and their solid solutions – photoluminescence and energy transfer. *J. Electrochem. Soc.* **1980**, *127*, 2234.

[112] Q. Bingyi, E. Banks, The binary system SrF_2-MgF_2 – Phase diagram and study of growth of $SrMgF_4$. *Mater. Res. Bull.* **1982**, *17*, 1185.

[113] N. Ishizawa, K. Suda, B. E. Etschmann, T. Oya, N. Kodama, Monoclinic superstructure of $SrMgF_4$ with perovskite-type slabs. *Acta Crystal. C* **2001**, *57*, 784.

[114] C. Veitsch, F. Kubel, H. Hagemann, Photoluminescence of nanocrystalline $SrMgF_4$ prepared by a solution chemical route. *Mater. Res. Bull.* **2008**, *43*, 168.

[115] G. Scholz, S. Breitfeld, T. Krahl, A. Düvel, P. Heitjans, E. Kemnitz, Mechanochemical synthesis of MgF_2 – MF_2 composite systems (M = Ca, Sr, Ba). *Solid State Sci.* **2015**, *50*, 32.